Summer 2010

Synthesis and characterization of microspheres for controlled release

Gurpartap Singh Sandhu

Department:

SYNTHESIS AND CHARACTERIZATION OF MICROSPHERES FOR CONTROLLED RELEASE

by

GURPARTAP SINGH SANDHU

A THESIS

Presented to the Faculty of the Graduate School of the

MISSOURI UNIVERSITY OF SCIENCE AND TECHNOLOGY

In Partial Fulfillment of the Requirements for the Degree

MASTER OF SCIENCE IN MECHANICAL ENGINEERING

2010

Approved by

Kimberly Henthorn, Co-Advisor
Anthony C. Okafor, Co-Advisor
L. R. Dharani

ABSTRACT

Synthetic hydroxyapatite (HAp, $(Ca_{10}(PO_4)_6(OH)_2)$ has always been of interest in medical applications because of its similarities to inorganic bone matrix. It has been used in biomedical applications for bone repair and substitution due to its biocompatibility. However, there are some differences in the stoichiometry, composition, and mechanical properties of human bone as compared to pure HAp. HAp particles have been successfully used as drug delivery carriers which deliver the drug to the affected part of the body and the remaining apatite gets degraded by the physiological processes in the body. In the present work, emphasis was on developing mechanically stronger HAp microspheres. Calcium lithium borate glass microspheres with 40 wt% calcium were reacted with phosphate (K_2HPO_4) buffered solutions under varying conditions of composition of glass, time, concentration, and pH to yield solid but porous HAp microspheres. DOE approach was used to analyze the effect of processing parameters on the reaction rate. The starting glass microspheres had diameters ranging from 150 to 355 μm and the reacted microspheres retained their shape and size. The microstructures of the reacted microspheres were examined using scanning electron microscopy (SEM). Chemical characterization of the reacted microspheres was also performed by X-Ray Diffraction (XRD), Energy Dispersive Spectroscopy (EDS), and Differential Thermal Analysis (DTA) studies. The as-reacted HAp microspheres were heat-treated at various temperatures which resulted in volume shrinkage of the microspheres and attributed to reduction in the porosity. Mechanical strength of as-reacted microspheres and heat-treated microspheres was tested by compressive load on an Instron Testing machine. The as-reacted microspheres had higher strength than as-reacted hollow HAp microspheres.

ACKNOWLEDGMENTS

Since the day I started working on this project, I have undergone significant transformation in my outlook towards research. I owe all my endeavors and hard work to my advisor, Dr. Kimberly Henthorn, who had immense faith in my capabilities. Her able guidance and undying encouragement always kept me going. Without her able support, I would not have been where I am right now. She never gave up on me in my bad times and taught me a lot about ethics. She has been highly instrumental in shaping up my thought-process and presentation skills. I owe her sincere thanks for what all she has done for me and I will always remember her for her pain-staking efforts in getting my thesis done.

I am thankful to Dr. Delbert Day for his patience and immense confidence in me when my research was not on track. He has been like a father figure who taught me a lot on personal level.

I highly appreciate the valuable feedback and timely reviews given by Dr. Anthony C. Okafor after sparing time out from his busy schedule. I owe special thanks to Dr. L.R. Dharani who let me know about this project in the first place.

I am thankful to Dr. Mohamed Rahaman, Dr. Richard Brow, Clarissa A. Wisner, Eric Bohannan, and Mo-Sci Corporation for their able assistance.

Last, but not least, I am thankful to my lovable parents and elder sisters who kept me going throughout this journey. I am also grateful to Ali Mohammadkhah, Sonali Kalghatgi, and Gautham Unni for being an inevitable part of my research group. Special thanks to Ali Mohammadkhah whose hard work was a source of inspiration for me.

TABLE OF CONTENTS

Page

LIST OF FIGURES

Figure Page

LIST OF TABLES

1. INTRODUCTION

1.1 OVERVIEW OF HYDROXYAPATITE

Calcium orthophosphate bioceramics form the basis of artificial implants used inside the body. A large number of bioceramics are derived from calcium orthophosphate which have compositional variability based upon hydroxyapatite, α-tricalcium phosphate (TCP), β-tricalcium phosphate, and biphasic calcium phosphate. Of the several calcium phosphates, hydroxyapatite (HAp, $Ca_{10}(PO_4)_6(OH)_2$) is an obvious choice for bone substitute because of its biocompatibility and its resemblance in structure and composition to the mineral phase of the bone [1,2,3]. Also, HAp phase is very stable in physiological conditions due to its lower solubility and lower resorption rates. Hence, HAp is the preferred choice for biological implants rather than α- and β-TCP [4,5].

The inorganic structure of the HAp devices account for their higher mechanical strength as compared to corresponding devices obtained from biodegradable polymers. Chemically, HAp is an important constituent of bone and does not produce any immunological reactions. However, the toxicity of fine HAp particles has been the subject of recent concern. Prior research has shown that solid or particulate HAp produces a favorable substrate for proper adhesion and proliferation of osteoblasts thereby resulting in more efficient growth of new bone [6,7], whereas fine particles or particulates of HAp produce an adverse effect on living cells due to their high surface area [8,9].

The size, morphology, and structure of the HAp particles affect their biological activity inside the body. Figure 1.1 shows both plate like elongated crystals and equiaxed crystals of HAp. HAp morphology can be varied from single crystalline sheets to rods to

equiaxed particles by changing the temperature and pH of the solution during precipitation reactions. Lower pH conditions give sufficient time for crystallization of HAp, which causes formation of elongated rod shaped structures, while higher pH conditions result in formation of equiaxed crystals. The properties of the HAp crystals are influenced by their morphology to a large extent directly or indirectly [10].

The apatite crystals that exist in bone are Ca-deficient and have a plate-shaped morphology [11]. The Ca/P ratio for stoichiometric HAp is 1.67. The biodegradability of the calcium phosphate ceramics depends upon the variability of Ca/P ratio between 1.5 and 2.0 [12]. HAp crystals, present in the bone in the form of crystals or plates, have a length of 40-60 nm, width of 20 nm, and thickness of 1.5-5.0 nm [13,14,15].

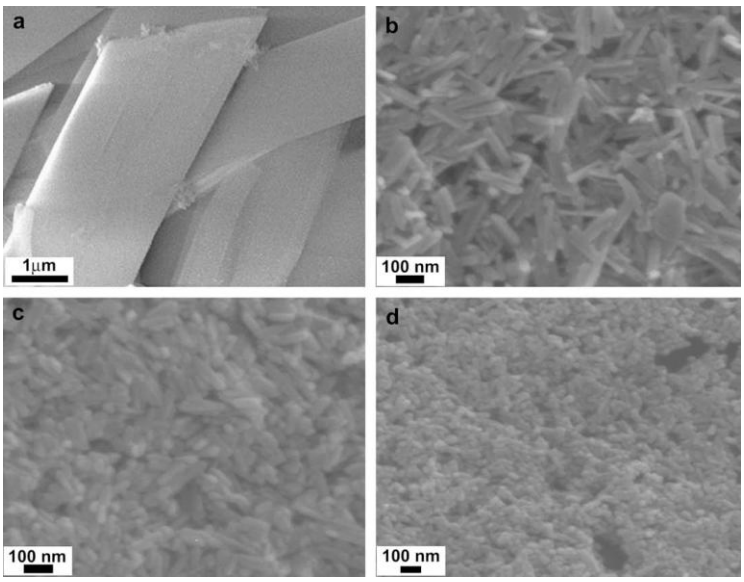

Figure 1.1: SEM micrographs of varying hydroxyapatite crystals processed under different pH conditions at 423K.

The inheritance of HAp from predecessor octacalcium phosphate (OCP) phase or amorphous calcium phosphate (ACP) phase is attributed as one of the reasons for the rod shaped morphology of HAp. Many experimental results have shown that OCP is formed in the initial stages of biomineralization and is further converted to HAp [16]. Kinetic studies show that OCP formation is much more favorable than HAp in simulated body fluids as the surface energy of HAP is much higher than the OCP phase, which allows conversion of OCP to HAp [17,18,19]. Prior research shows that HAP is the most stable phase of all the calcium phosphate phases in aqueous solutions with pH > 4.2. Also, it is the least soluble phase in such solutions [20].

HAp ceramics obtained from natural materials such as coral or bone have some inherent properties of the starting raw materials such as porosity, but they have comparatively different physical and chemical properties [21,22]. The clinical applications of HAp are sometimes limited due to its inherent brittle behavior [23]. Also, its potential to be used as graft material is not reliable in wet environments and it cannot be used in heavy load bearing applications such as artificial teeth.

1.2 MECHANICAL PROPERTIES OF HYDROXYAPATITE

HAp applications inside human body are limited due to its inherent brittle behavior. The mechanical properties of bioceramic implants comprised of HAp crystals should match the mechanical behavior of the tissue for the clinical success of the implant. Hard tissue replacements should have a modulus the same as or greater than that of bone [24]. The HAp microspheres developed in this research work were aimed at being used as drug delivery carriers inside the human body. The microspheres need to be strong

enough to allow sustained release of drug without them breaking apart. The scaffolds made from bioactive glasses used for implants inside the body should also be mechanically matched with the properties of the bone. The quantitative processing parameters for fabrication of artificial bone implants are largely decided by taking into account the mechanical properties of the hard tissues and bones at the site of implant. Generally, the mechanical properties of bone depend upon level of humidity, type of bone, direction of load application, and mode of applied load. Increasing human age causes a drastic decrease in the strength and volume of the bone [25]. Hence, the bone implant should be fabricated accordingly.

Hydroxyapatite is generally classified into two categories of dense hydroxyapatite and porous hydroxyapatite depending upon the extent of porosity, size of pores, and volume of pores with respect to the sample volume**.** In the case of dense HAp, the strength increases as the Ca/P ratio increases to the stoichiometric value of 1.67 but the strength decreases as the Ca/P ratio increases beyond 1.67 [26,27]. The compressive strength, as reported in the literature, is about 120 – 900 MPa [28,29]. The strength of dense HAp decreases exponentially with increasing porosity [29,30]. Dense HAp is generally more brittle (because of low value of its slow crack growth coefficient) so it cannot be used for high load bearing applications. Its strength reduces further drastically when it is implanted in wet conditions inside the body. Apart from sudden failure, HAp ceramics are very sensitive to slow crack growth behavior which occurs from pre-existing defects and have reduced lifetimes under stress. Thus, it is very important to determine the mechanisms involved in crack propagation in HAp ceramics in order to predict the lifetime of these materials for a given application.

On the other hand, porous hydroxyapatite has been widely accepted as a bone substitute because of its firmer mechanical fixation properties with hard tissues and bones. The minimum pore size required for bone ingrowth into a HAp implant is 100 μm which is fulfilled by porous HAp ceramics [30,31]. The biggest advantage of a porous structure is that it is light in weight and the porous network provides appropriate space for bone ingrowth into the implant. However, the necessity of such large pores decreases their strength but by changing the pore geometry, the strength of porous HAp can be controlled [32,33]. The difference between the elastic modulus values of HAp and bone accompanied by low inelastic ability of HAp attributes to greater stress concentration at the bone-material interface and enhances fracture [34]. The compressive strength, as reported in the literature, is about 2-100 MPa [35,36]. The advantage with porous HAp is that they are less fatigue resistant and the bone ingrowth rate is much faster in them [37]. Porous HAp implants are gradually replaced by bone and their gradual biodegradation is a prerequisite for artificial implants. Wide application of porous HAp in the medical industry is in the form of HAp granules and blocks. The applications include drug delivery systems and filling bone defects. In this research work, solid but porous HAp microspheres were used for drug delivery purposes which provide a much better sustained release of drug over an extended time period.

1.3 DEPENDENCE OF MECHANICAL PROPERTIES OF HYDROXYAPATITE ON POROSTIY

Porosity in any kind of artificial bone implant and drug delivery carrier is absolutely required for bone ingrowth and controlled drug release, respectively. A calcium orthophosphate bioceramic's total volume largely consists of microporosity and

macroporosity (about 70%) [38]. However, any porosity also reduces the strength and stiffness of the HAp ceramic. Hence, there must be a balance between the porosity requirements and mechanical property requirements for clinical success of artificial bone implants and drug delivery systems. The range of mechanical properties listed in the literature show that these properties are sensitive to synthesis and testing parameters [39]. The mechanical properties of HAp depend upon various factors like pore size and fraction, initial material purity, sintering temperature and time, sample volume, and phases present.

Mechanical characterization of porous HAp by conventional tensile and impact testing methods is unsuitable due to problems encountered in gripping test pieces which causes damage to the porous specimens. However, compression testing has been successfully adopted for testing of porous and dense HAp [36,40]. The compressive strength of the HAp particles is influenced by various parameters like porosity, grain size, synthesis conditions, sintering time and temperature, and extent of dissociation of HAp at higher temperatures. There is high degree of variability in the compressive strength of HAp ceramics prepared through same method [41].

1.4 OVERVIEW OF BIOACTIVE GLASSES

Controlled conversion of bioactive glasses to hydroxyapatite (HAp, $Ca_{10}(PO_4)_6(OH)_2$) has recently shown promise as a method of treating bone defects. Bioactive glass particles can potentially be used as bone fillers because they easily take the shape of the bone defect. Their bonding properties are enhanced due to their high specific surface area and porous structure [42].

The surface of the bioactive glass undergoes a gradual kinetic modification upon implantation in the body fluids thereby forming a biologically active hydroxycarbonate apatite (HCA) layer. This layer forms an interfacial bond with living tissues. Formation of HAp surface layers have been reported upon immersion of calcium borosilicate glasses in simulated body fluids [43]. Wojick's [44] proof of formation of an HAp layer on calcium borate glasses without silica upon immersion in 0.25 M and 1.0 M phosphate solutions discarded the theory that a silica gel layer was necessary as a nucleation site for amorphous calcium phosphate (ACP) to crystallize to HAp [45].

Precipitation from aqueous solutions, solid-state reactions, hydrolysis of calcium phosphates, and hydrothermal methods are most common chemical methods for preparation of HAp [1]. Depending on the type of synthesis, materials with varying morphology, levels of crystallinity and stoichiometry can be obtained. Highly crystalline and stoichiometric HAp compositions can be obtained by solid-state reactions, but processing is cumbersome, involving higher temperatures and longer heat treatment durations [46,47]. Generally, HAp processed by precipitation from aqueous solutions technique is calcium-deficient ($Ca_{(10-x)}(HPO_4)_x(PO_4)_{(6-x)}(OH)_{(2-x)}$) and has low crystallinity [48]. HAp crystal morphology, as a result of the precipitation reactions, is generally in the form of sharp needles, rods, or equiaxed particles. As a result of this precipitation technique, a layer-by-layer reaction takes place resulting in formation of unstable OCP phase which transforms to the ACP phase rapidly. As the reaction progresses, ACP gradually transforms to amorphous calcium deficient hydroxyapatite which further transforms to a very crystalline calcium deficient HAp.

The Ca/P molar ratio of the precipitated HAp can be closer to stoichiometric HAp if the pH of the phosphate solution is maintained constant during the reaction [49]. Reaction temperature greatly influences the conversion rate from ACP to HAp. Raising the temperature accelerates the formation of crystalline HAp and hence, shortens the reaction time [50]. The reaction temperature also affects the particle size and morphology of the crystalline HAp.

The non-uniform manner in which alkali borate glasses convert to HAp is advantageous for controlled drug delivery purposes and other medical applications. The non–uniform reaction is advantageous because it is a novel method of forming highly porous gels at low temperature (< 100ºC) glass-solution reaction. This "solid-gel" method is superior to the conventional method of preparing porous materials which involves high temperature "burn-out" steps. In addition, the size of a microsphere does not change as the non-uniform reaction proceeds. Because of its excellent biocompatibility, the side effects of using these microspheres *in vivo* are minimal. Based on the starting composition of alkali borate glasses, the conversion process can yield hollow or solid but porous microspheres of HAp. Hollow and porous HAp microspheres can be filled with a liquid drug by immersing the microspheres in the liquid and then evacuating the gas from the hollow core and the pores within the microshell. The drug-loaded microshells can further be used inside living bodies for various medical applications.

Fears [51] showed that calcium lithium borate glasses containing less than 40 wt% calcium oxide resulted in the formation of hollow microspheres whereas glasses containing greater than 40 wt% calcium oxide formed solid but porous microspheres.

The transformation process depends upon the composition of the starting borate glass, temperature, and composition of the surrounding liquid [52]. The main goal of this work was focused on calcium lithium borate glasses containing 40 wt% calcium oxide. The solid but porous microspheres have an advantage of being superior in mechanical strength to the hollow microspheres. The porosity of the porous microspheres can be controlled by the extent of heat treatment at a chosen temperature. By changing the porosity in this way, it is possible to control the rate at which drug is released from the microspheres.

1.5 KINETICS OF BIOACTIVE GLASS CONVERSION

The bioactive glasses react in simulated body fluids to form bonding material (hydroxycarbonate apatite) which can bond to the bone and living tissues. The non-uniform dissolution of glasses occurs due to a sequence of reactions starting at the surface of the glass when immersed in phosphate buffered solution. The mechanism of growth of the HAp layer seems to be accelerated by the presence of hydrated silica in silicate glasses (like Na_2O-CaO-SiO_2). A selective ion exchange process is responsible for the non-uniform dissolution of the glasses containing silica [53].

On the contrary, when borate glasses are immersed in phosphate buffered solution, a bulk reaction initiates as both the glass former and alkali oxide are released from the alkali borate glass thereby dissolving in the solution. The dissolution of lithium borate glasses has already been supported by a thermodynamic model which is based on the solubility of the oxides comprising the glass [54]. Also, a model has been proposed which describes the three-step dissolution which occurs during any chemical dissolution

process [55]. When calcium lithium borate (CaLB3) glass is immersed into phosphate buffered solution, the H_3O^+, H_2O, and OH^- ions react with soluble LB3 component of the glass [56,57]. The following reactions start when LB3 component starts dissolving in the solution.

$$B_2O_{3(s)} + 3H_2O_{(liq)} \leftrightarrow 2H_3BO_{3\,(aq)}$$

$$Li_2O_{(s)} + H_2O_{(liq)} \leftrightarrow 2Li^+_{(aq)} + 2OH^-_{(aq)}$$

As a result of the above reactions, Li^+ and H_3BO_3 are released into the solution as a consequence of hydrolysis reactions. The phosphate buffered solution enters the glass matrix thereby leading to the expansion of solute. Simultaneously, Li^+ and H_3BO_3 mix with PBS solution causing expansion of the solvent [53]. The expanded stable Ca^{2+} ions interact with the PO_4^{3-} ions which enter the vacant volume created by leaving Li^+ and H_3BO_3 from the glass, immediately reacting with phosphate anions to form a calcium phosphate or calcium hydroxide phase. The calcium phosphate phase formed by such solution processes is amorphous in nature, similar to most sol-gels prepared by precipitation technique [58]. The low solubility limit of $CaPO_4$ is the reason for formation of amorphous $CaPO_4$ when Ca^{2+} and PO_4^{2-} ions are together in a solution. Fears [51] reacted various compositions of CaLB3 glass microspheres containing varying amounts of CaO (5 wt % through 50 wt %) in phosphate buffered solutions. The following (Figure 1.2) is the schematic depiction of the non–uniform reaction that CaLB3 microspheres (CaO wt% < 40) undergo in the phosphate buffered solution.

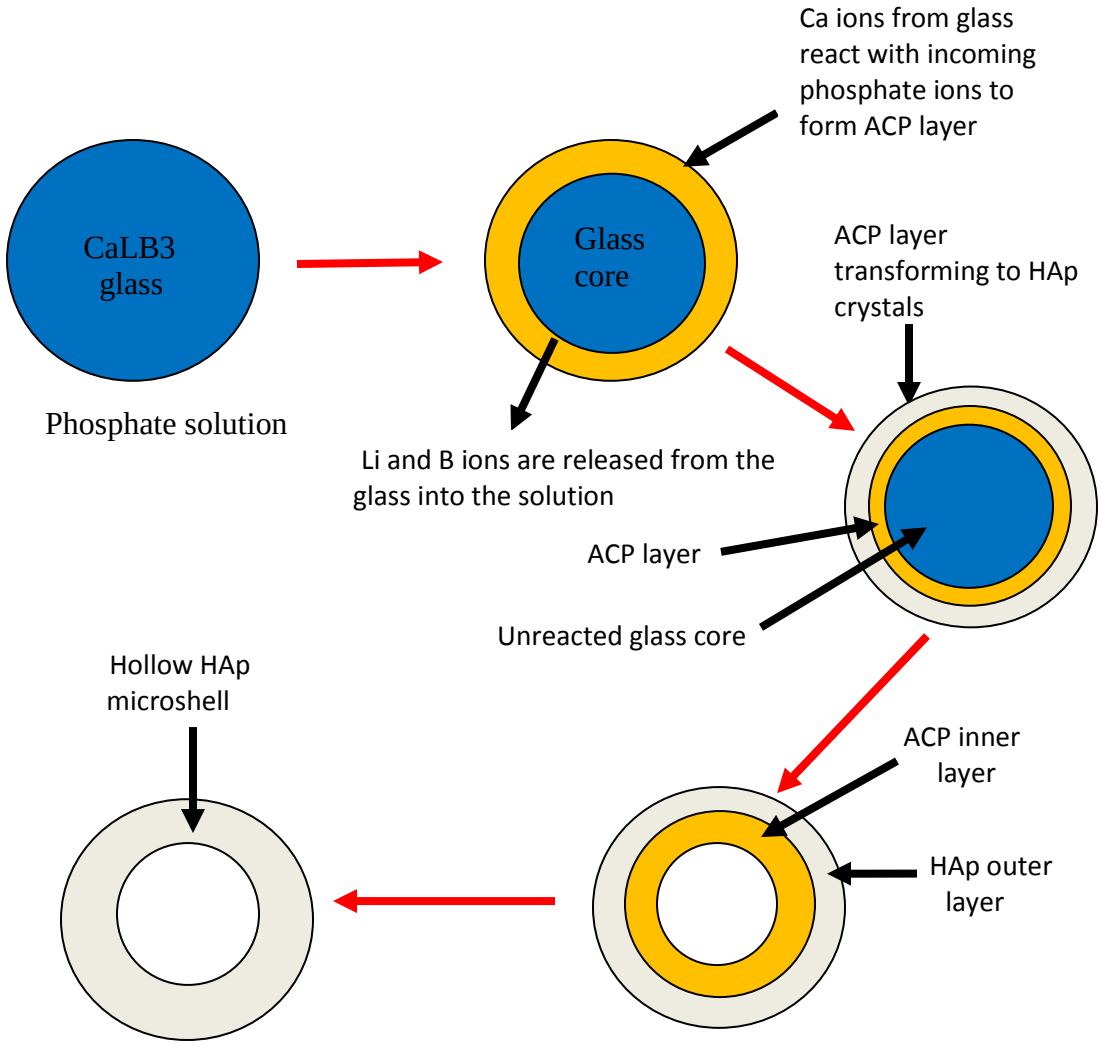

Figure 1.2: Schematic representation of reaction of CaLB3 (less than 40 wt% calcium content) microspheres in phosphate buffered solutions [51].

He found that glasses containing less than 40 wt% CaO yielded hollow microshells, whereas glasses containing greater than 40 wt% CaO yielded solid but porous microspheres upon reaction (Figure 1.3). When CaLB3 glasses containing less than 40 wt% CaO are immersed in PBS solutions, hollow microshells are formed with the thickness of the shell depending upon the amount of calcium in the starting glass. The

reaction starts at the surface of the glass microspheres and the reacted surface acts as a nucleation site for further growth of solid phases [59].

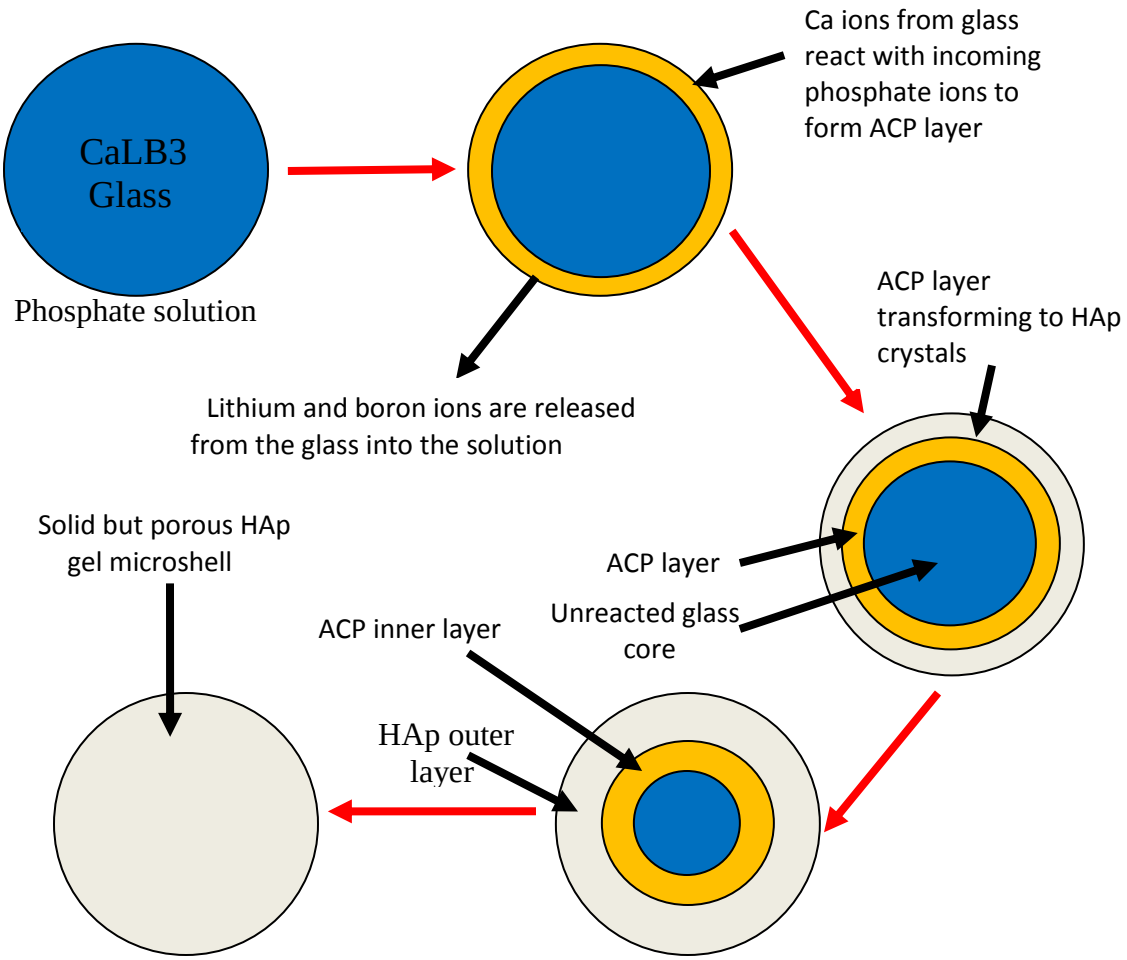

Figure 1.3: Schematic representation of reaction of CaLB3 (≥ 40 wt% calcium content) microspheres in phosphate buffered solutions.

For small proportions of calcium in the glass, the shrinking core of reacting CaLB3 glass becomes separated from amorphous calcium phosphate layer after certain layer of reaction (due to convection currents produced by aqueous species entering into the glass). The reason for this separation is insufficient amount of Ca^{2+} ions liberated from reacting glass to form a continuous layer during the reaction which results in the

formation of a void. As the calcium content increases from 5 wt% to 40 wt%, the slower reaction kinetics yield weaker convection currents at the glass/gel interface, and no core detachment occurs for high calcium content. As a result, solid but porous microspheres are obtained for CaLB3 glasses containing more than 40 wt% CaO [53].

1.6 EFFECT OF SINTERING ON THE PROPERTIES OF HYDROXYAPATITE

Sintering seems to play an important role in producing bioceramics with desirable properties. Stea [60] showed that sintered HAp forms very tight bonds with the bone tissue. Several processes occur during the sintering process which are as follows:

1. Dehydroxylation involving removal of moisture from ACP in the form of gaseous products along with volatile chemicals (if any).
2. Dense HAp ceramics are formed proceeding removal of gases accompanied by shrinkage of the samples until the ceramics are sintered.
3. Concurrent reduction in the specific surface area along with increase in crystal size.

Sintering causes an increase in the toughness and mechanical strength of HAP ceramics [61,62,63]. The sintering temperature and duration has a significant effect on the density, porosity, grain size, bonding between the grains, chemical composition, and strength of the HAp bioceramic. The sintering temperature is a critical factor that influences the densification behavior, sintered microstructure, hardness of HAp, and phase stability.

It has been found that the grains of calcium deficient HAp start coalescing at a temperature below 1000ºC without much densification [64]. Particle coalescence is

generally associated with a decrease in the specific area. The temperature at which the particles begin to coalesce generally depends upon the Ca/P ratio. As the Ca/P ratio decreases, the coalescing temperature also decreases and the Ca-deficient HAp dissociates into a biphasic mixture of stoichiometric HAp and tricalcium phosphate (TCP). The final microstructure and extent of sintering in the resultant ceramic depends upon the proportion of HAp and TCP in the biphasic mixture [65]. Dissociation of HAp attributes to volume diffusion and grain boundary diffusion in the microstructure thus causing densification of the matrix volume [66].

Pressure less sintering of HAp powders can result in attainment of theoretical density at 1000-1200ºC [67]. Higher temperatures (~ 1250-1400ºC) result in exaggerated grain growth and irreversible decomposition of HAp because HAp is unstable at such high temperatures [68,69]. Such high temperatures cause decomposition of hydrated HAp to anhydrous calcium phosphates like tri-calcium phosphate (TCP) [70]. Generally, dehydroxylation of HAp beyond a critical point leads to its decomposition. The critical point refers to a temperature value typically in the range of ~1250-1400ºC. The actual value of this critical value depends upon the type of HAp material [70]. Some prior research in the effects of sintering on dense hydroxyapatite yielded the following results as listed in Table 1.1.

Table 1.1: Effect of sintering temperature on dehydroxylation of HAp [71]

Sintering temperature range	Effect
< 800ºC	Slower dehydroxylation
800ºC - 1350ºC	Enhanced dehydroxylation
> 1350ºC	Irreversible dehydroxylation leading to decomposition

The effect of sintering temperature on the microstructure has also been elaborated in some prior research work. There is quite less densification at temperatures below 900˚C but particle coalescence starts in this range. Majority of densification occurs in the temperature range of 900˚C-1150˚C. Blowholes start appearing at a temperature of 1200˚C and increase in number and size as the temperature is increased up to 1350˚C [71]. Blowholes are the isolated pores created due to exudation of some traces of gas trapped inside the HAp matrix.

The decomposition process of HAp bioceramics is a function of the partial pressure of water vapor in sintering atmosphere. Sintering under vacuum causes earlier decomposition whereas sintering under high partial pressure of water vapor prevents the decomposition. However, the presence of water in a sintering atmosphere inhibits the densification process of HAp and causes accelerated grain growth [72].

1.7 DIFFERENT TECHNIQUES OF SINTERING

Various sintering techniques have been developed until now which can be broadly classified into three groups, namely sintering in conventional furnaces, microwave sintering, and spark plasma method. The most practical procedure of sintering is by using a conventional programmable furnace (used in this research work). However, low heat conductivity and high shrinkage of HAp samples generate thermal and residual stress fields with this method. In addition, conventional sintering can be a time consuming process for larger samples as they require a lower heating range which is achieved by using a longer sintering cycle [41]. The traditional techniques of sintering involve exposure of HAp ceramics to higher temperatures for longer durations for

consolidation of HAp particles, which often results in surface contamination and further degradation of the desired mechanical properties.

Sintering in a microwave has the advantage of uniform heating of the specimen across its volume which eliminates the stresses due to non–uniform shrinkage. The problem with microwave sintering is measurement of the temperature of the sample. Prior to sintering, a thermocouple is placed as close as possible to the sample. However, shrinkage of sample with time increases the initial gap between thermocouple and sample thereby causing interference of electric field with the thermocouple signal. Another problem, with microwave sintering is dependence of sample temperature on the density of the samples which requires power adjustments during the sintering process [41].

New techniques such as hot pressing, hot isostatic pressing, and spark plasma sintering decrease the temperature of the densification process, decrease the exaggerated grain size, and achieve higher densities, thereby leading to finer microstructures, better thermal stability of ceramics, and improved mechanical properties. The problem with new techniques of sintering is that they produce HAp ceramics with high relative densities which make biocompatibility difficult and complicates the process of cell proliferation.

1.8 MEDICAL APPLICATIONS OF BIOCERAMICS

The difference of bioceramics from other classes of materials is their ability to remain in a biological environment without producing any damaging effect on the environment and without becoming damaged themselves. Ceramics and glasses have been used in a wide range of health industries namely eye glasses, tissue culture flasks,

thermometers, and fiber optics for endoscopy. Insoluble porous glasses act as carriers of enzymes and antibodies inside bodies since they are resistant to microbial attacks, pH conditions, and solvent conditions [73]. Tissue bonding to bioactive ceramics is an evolving field that can result in the design of bioceramics for interfacial bonding with soft and hard tissues.

Conventional drug delivery systems are in the form of pills and capsules. They can be effective to treat an ailment but are not very efficient as they are metabolized by the body very rapidly. Hence, there is a short burst of overmedication, which is followed by a longer period of under-medication [74]. This necessitates the need for a controlled drug delivery vehicle that slowly releases a therapeutic concentration of drug at the site of treatment over longer durations of time. This slow drug release increases the efficiency of the drug thereby decreasing the side effects of the drug and eliminates short bursts of overmedication prevalent in conventional drug delivery systems.

The biggest advantage of HAp microspheres is that they can be used as drug-delivery carriers because of their porous or hollow microstructure. Alkali borate glasses doped with rare earth element oxides have been transformed into biologically useful materials, which have been used as radiation delivery vehicles to treat rheumatoid arthritic joints [52]. Porous hydroxyapatite microspheres are appropriate for controlled drug delivery purposes because they can be processed with continuous porosity from bioactive glasses.

The HAp microspheres are chemically similar to human bone and have a pore size < 200 nm in diameter [43]. The porosity of the microspheres allows loading them with liquid drug by vacuum impregnation and then implanting them in the body so that

the sustained release of the drug from the HAp matrix can treat the diseased part over an extended time period. Also, the biodegradability of these microspheres is an added advantage. Since HAp is biodegradable; the physiological processes in the body would slowly remove the HAp microspheres from the body after the drug delivery is finished. HAp is an obvious choice for bone substitute because of its biocompatibility and its resemblance in structure and composition to the mineral phase of bone [1,2,3]. Also, use of HAp inside the body has been approved by Food and Drug Administration (FDA) [74].

Another feasible medical application of porous HAp microspheres is using rare earth hydroxides to deliver radiation and chemotherapy to malignant tumors [53]. It involves reaction of dysprosium lithium borate bioactive glasses with saline solution to form porous microspheres of dysprosium hydroxide. The porous microspheres are then neutron activated to beta emitting ^{165}Dyradioisotope in a nuclear reactor. The radioactive porous microspheres are further loaded with a chemotherapeutic drug and injected at the tumor site. The delivery of localized radiation from a short lived ^{165}Dy radioisotope would treat the tumor and after the radiation has decayed, the controlled release of drug would continue to treat the malignant tissue for extended time period. Hence, delivery of radiation and drug from porous dysprosium hydroxide microspheres forms a complete biodegradable system.

Porous hydroxyapatite materials are also used for catalyst support media because of their high specific surface area and porosity [53]. Hollow microshells of HAp can be used for acoustic imaging by filling the core with gas surrounded by impermeable walls [76]. Other applications of bioceramics include hip and teeth replacement, spinal fusion,

bone fillers after tumor surgery, and augmentation and stabilization of the jawbone. Composites having the same toughness and elastic modulus as that of human bone are being developed.

2. EXPERIMENTAL PROCEDURE

2.1 GLASS PREPARATION

Calcium lithium borate (CaLB3) glasses are a type of alkali borate glass in which all the elements are present in their oxide forms. In these glasses, B_2O_3 acts as a glass former and Li_2O is a flux, which helps to reduce the melting temperature. CaO acts as a property modifier and modifies the chemical durability and viscosity. All CaLB3 glasses prepared in this work had a Li_2O:B_2O_3 molar ratio of 1:3, and were formed from reagent grade $CaCO_3$, Li_2CO_3, H_3BO_3, and $CaSO_4$ powders.

CaLB3 glasses are denoted according to the weight percentage of CaO they contain. For example, CaLB3 glasses containing 40 wt% CaO are named CaLB3-40. Glass microspheres obtained from Mo-Sci Corporation, synthesized by Fears, and self-prepared on campus are further labeled with the notations "-MoSci," "-Fears," and "-SX," respectively, where X represents the weight percentage of CaO coming from $CaSO_4$ with the balance coming from $CaCO_3$. Table 1 lists the sources and size ranges of glass microspheres used for conversion reactions in this work. The size range in Table 2.1 specifies the mesh openings of the sieves used to classify particles e.g. +45/-106 indicates that 90% or more of the particles will be retained by 45 μm opening sieve and 90% or more of the particles will pass through 106 μm opening sieve.

Table 2.1: Various starter glasses used for conversion reactions.

Glass Identifiers	Source	Size Range (μm)
CaLB3-20-MoSci	Mo-Sci Corporation	+45/-106
CaLB3-40-MoSci	Mo-Sci Corporation	+45/-106
CaLB3-40-Fears	Prepared by Fears	+106/-212
CaLB3-40-SX	Prepared by Sandhu	+150/-355

Five compositions of CaLB3-40-SX glass microspheres were prepared with 0, 25, 50, 75, and 100 weight percentages of CaO coming from $CaSO_4$. Table 2.2 shows the weight percentages of respective oxides in CaLB3-40-SX glass identifiers. The reagent grade powders used in the preparation of glass compositions listed in Table 2.2 were calcium carbonate ($CaCO_3$), calcium sulfate ($CaSO_4$), boric acid (H_3BO_3) and lithium carbonate (Li_2CO_3).

Table 2.2: Various compositions of CaLB3-40 glass particles prepared on campus.

Glass Composition / Glass Identifiers	CaO wt% (from $CaCO_3$)	CaO wt% (from $CaSO_4$)	Li_2O wt%	H_3BO_3 wt%
CaLB3-40-S0	40.00	0.00	7.50	52.50
CaLB3-40-S25	30.00	10.00	7.50	52.50
CaLB3-40-S50	20.00	20.00	7.50	52.50
CaLB3-40-S75	10.00	30.00	7.50	52.50
CaLB3-40-S100	0.00	40.00	7.50	52.50

The raw materials for each glass were mixed thoroughly with a mortar and pestle and melted in a platinum crucible at 1100ºC for approximately 60 minutes. All the glasses except for the CaLB3-40-S0 glass formed a liquid melt after 1 hour. The CaLB3-

40-S0 glass did not form a liquid melt at all even after heating it up to 1300ºC for 1 hour. This may be due to large bubbles of CO_2 trapped inside the glass. When glass is melted, the carbonates decompose to CO_2 producing a large volume of bubbles that need to be removed from the melt. The bubbles can also form due to the physical entrapment of atmospheric gases during melting. These bubbles can be removed by allowing them to physically rise to the surface of the melt or by using fining agents. $CaSO_4$ acts as a good fining agent due to the fining property of SO_4^{2-} which reduces to SO_2 at higher temperatures. When $CaSO_4$ is used as a reagent grade powder, it decomposes at high temperatures and large quantities of SO_2 gas produced in the melt sweep away small bubbles which rapidly rise to the surface of the melt. SO_2 bubbles thus fine the liquid glass melt by removing the trapped CO_2 from the glass network and reducing the crystallization tendency of the melt [79]. This indicates that $CaSO_4$ and $CaCO_3$ must be present in adequate proportions when preparing high CaO content glasses. Some fining agents remove oxygen from the already present bubbles thereby reducing them below their critical size and hence, surface tension eliminates the smallest bubbles.

Liquid melts of CaLB3-40-S25 through CaLB3-40-S100 glasses were quenched between two cold stainless steel plates at room temperature to prevent crystallization. The quenched glass was then ground with a mortar and pestle and the irregular glass particles were dry sieved to 150-355 μm. The particles were shaped into glass microspheres in a drop tube furnace. The drop tube apparatus consisted of a small dense mullite tube (inner mullite tube in Figure 2.1) that extended into the vertical drop tube furnace within a large dense mullite tube. The top of the furnace was sealed with insulation to prevent particles from being entrained by the hot air. The furnace was

heated to ~1130ºC and the irregular particles were dropped from a vibrating spatula into the small tube.

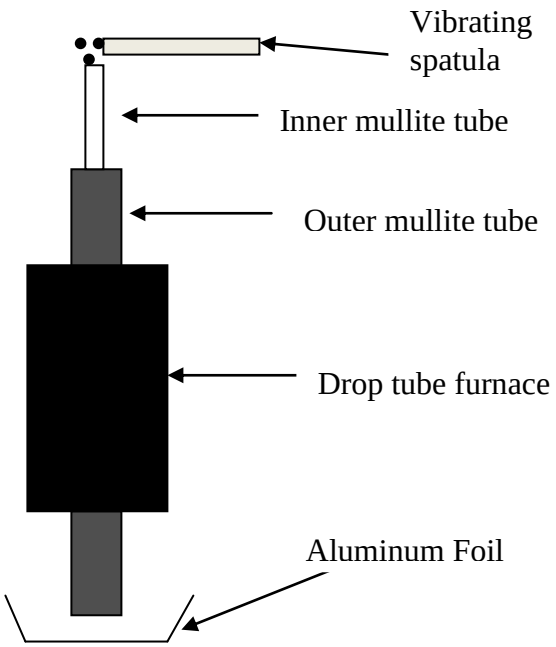

Figure 2.1: Vertical drop tube furnace used for spheridization of glass frit.

As the irregular particles passed through the hot zone of the furnace, they melted and surface tension pulled them into microspheres. The particles obtained at the bottom of the furnace were collected in aluminum foil and allowed to cool to room temperature. The microspheres were then stored in small glass vials for further reaction and characterization.

2.2 CHEMICAL REACTION OF GLASSES

The glass microspheres were reacted in phosphate buffered solutions at varying concentrations, pH values, and time durations in order to achieve complete conversion to HAp. The microspheres were reacted in 1000 mL Pyrex® beakers and 250 mL Kimax®

flasks. Equation (1) was used to calculate the volume of solution required to react 1 g of glass in a given concentration of solution:

$$0.1 = M * V \text{ ---------- (1)}$$

where M = molarity of the phosphate solution and V = volume of the phosphate solution.

Equation 1 is based on 50 mL of 0.25 M K_2HPO_4 solution per 1 g of CaLB3-5 glass such that the concentration of PO_4^{3-} ions in the solution exceeded the concentration of Ca^{2+} ions by at least 15:1 [51]. The volume of solution increased with increasing calcium content of the glass. The concentration of PO_4^{3-} ions in the solution was kept high so that the overall concentration of PO_4^{3-} ions in the solution did not change significantly as they were consumed by the Ca in the glass. Hence, the solubilities of HAp and other calcium phosphate phases formed during the reaction were not affected.

CaLB3-20-MoSci glass microspheres were reacted at 37°C in 0.25 M K_2HPO_4 solution at pH = 9 (± 0.05) for 2 days. CaLB3-40-MoSci glass microspheres were reacted under the conditions listed in Table 2.3. The pH of the phosphate solution used to react CaLB3-40-MoSci microspheres was 12 (± 0.05). The CaLB3-40-Fears glass microspheres were reacted in a 0.25 M K_2HPO_4 solution at pH = 12 (± 0.05) at 37ºC for 2 days.

Table 2.3: Reaction scheme for CaLB3-40-MoSci glass microspheres.

Concentration of phosphate solution	Temperature	
	37˚C	70˚C
0.25 M	4 days and 10 days	2 days and 4 days
0.50 M	4 days and 10 days	2 days and 4 days

The pH of the phosphate solution was adjusted using 2 M NaOH and HCl solutions. The microspheres were reacted in 1000 mL Pyrex beakers placed on a heating plate to maintain them at a constant temperature. The solution was continuously stirred with an overhead stirrer and the beaker was covered with paraffin film to prevent loss of solution. An overhead thermocouple was inserted in the solution to monitor the temperature.

The main emphasis of this research was on preparing and reacting CaLB3-40-S50 and CaLB3-40-S75 glass microspheres. CaLB3-40-S50 glass microspheres were reacted in 0.25 M, 0.50 M, 0.75 M and 1.00 M K_2HPO_4 solutions at pH=10 (± 0.05) and 37ºC. The reactions were carried out for 6 days and 12 days at each concentration level. In addition, the CaLB3-40-S75 glass microspheres were reacted in K_2HPO_4 solution pH=10 at 37ºC at 0.5 M and 1.0 M concentrations for 6 days and 12 days at each concentration. In order to conclude the effect of pH on the microstructure, CaLB3-40-S75 glass microspheres were reacted in 1.0 M K_2HPO_4 solution at pH=8 and 12 (± 0.05) for 6 days at 37°C. The CaLB3-40-S50 and CaLB3-40-S75 glass microspheres were reacted in 250 mL Kimax® beakers. The beakers were placed in a sand bath mixer which was maintained at 37ºC and continuously shaken.

After the completion of all the reactions listed above, the solution was decanted and the microspheres were rinsed in three stages. The first stage involved thorough rinsing of the microspheres three to four times with deionized water. The second stage involved rinsing the particles in an equal volume mixture of ethyl alcohol and de-ionized water three times. The third stage involved washing the microspheres with pure ethanol

twice to dehydrate the rinsed microspheres. The washed microspheres were dried in an oven at 90ºC for approximately 48 hours and stored in glass vials until needed.

2.3 HEAT-TREATMENT OF REACTED MICROSPHERES

Completely converted CaLB3-40-S50 microspheres were heat-treated in a Barnstead Thermolyne furnace. Approximately 100 mg of microspheres were placed in a platinum crucible and heat-treated at 300^{o}C, 600^{o}C, 900^{o}C, and 1200^{o}C for 1 hour. A heat ramp rate of 10^{o}C/min was used.

2.4 MICROSTRUCTURAL ANALYSIS

The as-reacted microspheres and heat-treated microspheres were imaged using a Hitachi S570 scanning electron microscope (SEM) equipped with a LaB_6 filament and Hitachi Field Emission S4700 SEM. Carbon tape was placed on metal SEM mounts and the particles were sprinkled onto the mount with a spatula. The mount was placed under a Carl Zeiss optical microscope and X-ACTO blades were used to cut open the microspheres to look at the cross-section under SEM. After cutting the microspheres, the sample mounts were sputter-coated with gold/palladium and carbon to form a conductive layer and prevent charging of samples when put inside the scope. The samples were analyzed on the Hitachi S-570 SEM at magnifications up to 8000X. The S-570 SEM was equipped with the Revolution® software which was used to capture images. The high magnification images were taken on an S-4700 SEM at magnifications up to 100,000X.

2.5 CHARACTERIZATION OF REACTED MICROSPHERES

2.5.1 Energy Dispersive Spectroscopy Analysis and X-ray Mapping. Energy Dispersive Spectroscopy (EDS) is an analytical technique that helps in identification of the elements present in the sample thereby providing information about the elemental composition. EDS systems are most commonly attached to SEM probes and are based on the operating principle that emittance of X-rays from an element are characteristic of the atomic structure of that particular element. The emitted X-rays vary for different elements due to the variations in the atomic structure. During their operation, the sample interacts with a focused beam of electrons, and X-rays emitted from the sample are analyzed by the EDS detector. Generally, the atom in an element is in an unexcited state and the electrons in various shells are in their ground states. Once an atom is hit by an electron beam, the electron from an inner lower energy shell of the atom is ejected and an electron from an outer higher energy shell fills the empty hole created by the outgoing electron. Hence, the X-rays are emitted from the atom that are characteristic of the difference in the energy between high-energy shell and lower-energy shell. This X-ray signal is then converted to a voltage signal within the detector, which is further sent to a pulse processor and the data are displayed on the monitor for analysis.

Figure 2.2 shows a representative EDS spectrum. The EDS spectrum demonstrates elemental peaks with X-ray energy levels on the horizontal axis and counts per second on the vertical axis. The EDS spectrum of a single element exhibits series of peaks due to large number of electrons in the atom that can jump between various energy levels. The peaks in the EDS spectrum refer to the electron orbital shells they represent and are denoted as K, L, and M peaks. Higher atomic number elements appear on the

right hand side of the plot whereas elements with lower atomic numbers appear on the left hand side of the plot. The EDS spectrum can be interpreted as follows:

1. The presence of a peak corresponding to an element confirms the presence of that element in the sample.

2. Elements present in greater concentration are represented by higher peaks and presence of more than one peak corresponding to an element is possible.

3. Quantitative analysis can provide weight and atomic percentages of the elements present.

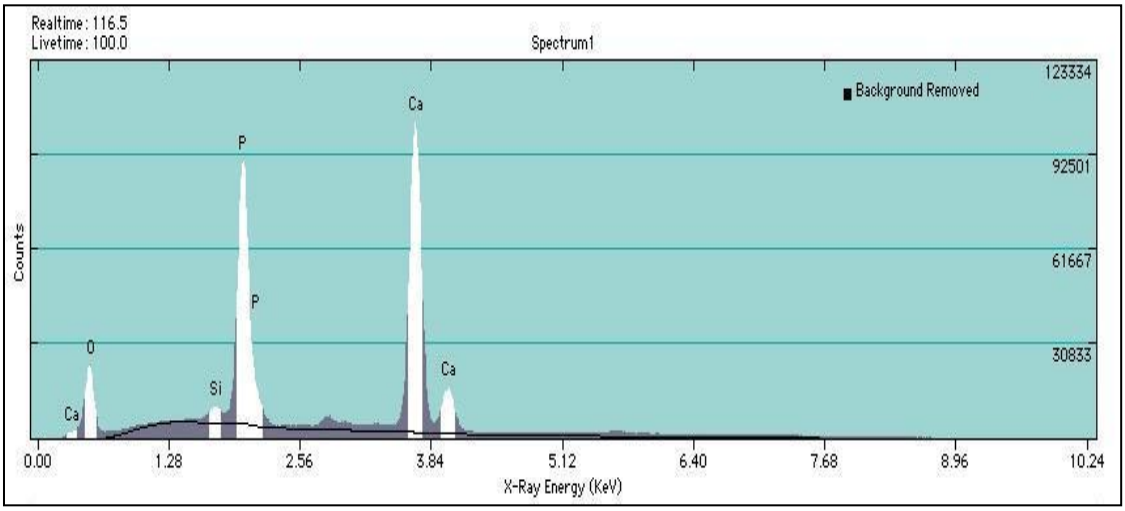

Figure 2.2: EDS spectrum showing calcium and phosphorus elemental peaks.

The Hitachi S-4700 SEM is equipped with an EDAX Phoenix system for the EDS analysis and the Hitachi S-570 SEM is equipped with a Silicon Drift Detector (SDD). The advantages of using SDD include:

1. Requiring less acquisition times accompanied by higher count rates (> 100,000 counts per second) that are due to higher X-ray signals from the sample.

2. No requirement of liquid nitrogen for cooling.

3. Higher resolution of elemental peaks.

4. No problem of peak broadening with change in count rate.

5. Highly precise X-ray maps.

6. Able to detect lighter elements up to Be.

Phase maps (or X-ray maps) and elemental maps are colored maps retrieved for the elements obtained in the EDS spectrum. These maps are evidence of the extent of reaction in this work. Color codes can be designated to the corresponding elements and hence colored X-ray maps are obtained for different frame sizes as per choice (64x64, 128x128). A bigger frame size will give X-ray maps with higher resolution. An example of an X-ray map is illustrated in Figure 2.3:

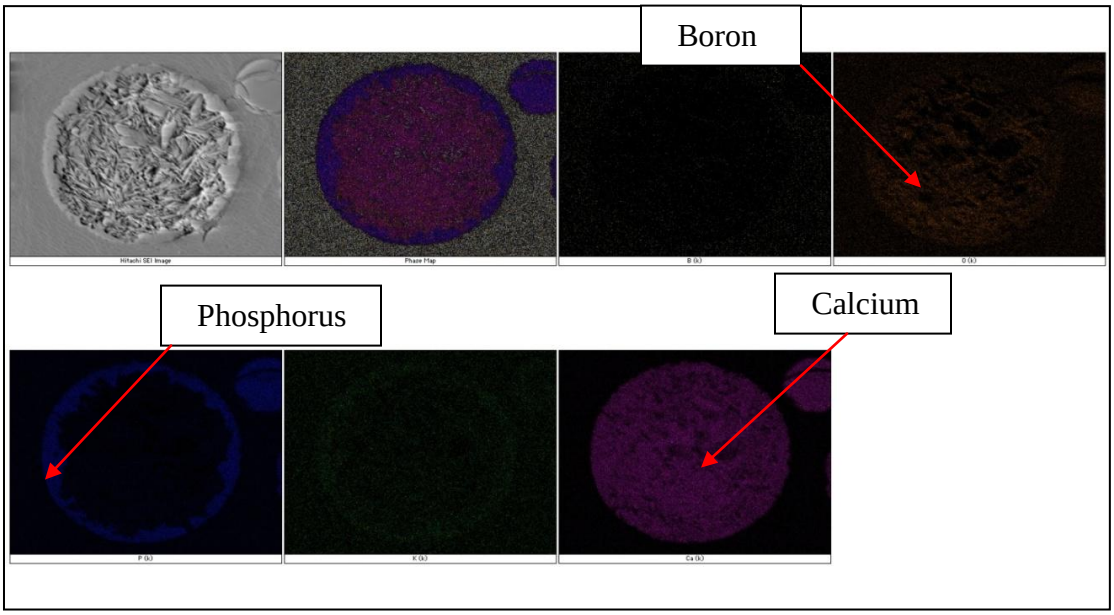

Figure 2.3: X-ray maps showing extent of reaction for reacted CaLB3-40-Fears microspheres.

Reacted CaLB3-40-Fears microspheres were mounted in epoxy resin and allowed to dry at room temperature for two days. The dried epoxy samples were mechanically polished with different SiC grit papers, beginning with 240 grit (53 microns) and finishing with a 3 microns fine diamond polishing suspension. The X-ray map in Figure 6 shows reacted CaLB3-40-Fears epoxy mounted microspheres. The mechanical polishing of the epoxy samples yielded a flat cross-section for which X-ray maps could be easily retrieved. The S-570 SEM was used to obtain X-ray maps for reacted CaLB3-40-Fears microspheres, and the S-4700 SEM was used to obtain EDS results and X-ray maps for reacted CaLB3-40-SX microspheres.

2.5.2 X-ray Diffraction and Differential Thermal Analysis. Crystalline phases in the reacted microspheres were identified with a Phillips X-ray diffractometer. X-ray diffraction measurements were obtained with a PANalytical X'Pert Multipurpose diffractometer utilizing Cu Kα radiation (0.15418 nm) and a PIXcel detector consisting of 255 active channels and an active length of 3.347^{o}. Data acquisition was obtained with a counting time of 150 seconds and a step size of 0.0263 degrees. XRD analyses for the reacted microspheres were compared with the standard XRD pattern for stoichiometric HAp.

Reacted CaLB3-40-S50 microspheres were heat-treated in a Netzsch STA 409 simultaneous thermal analyzer to determine any phase changes of HAp upon heating. Weight loss of the reacted microspheres was measured by thermo gravimetric analysis (TGA). Approximately 70 mg of reacted microspheres were heated in an Al_2O_3 crucible to a temperature of 1250°C in air at 10°C/min.

2.5.3 Compressive Strength of Reacted Microspheres. The rupture strength of the microspheres was first measured by using an Agilent Technologies® Nano-Bionix Universal Testing Machine (UTM). A schematic of the important functional elements of the instrument is shown in Figure 2.4. The two significant components of the instrument are the crosshead and the Nano Mechanical Actuating Transducer (NMAT column), both of which are controlled by a proprietary computer program named Test Works 4.0®. The crosshead is driven by a precision lead screw. It has relatively large range of motion of 150 mm with a resolution of 35 nm. However, most of the system's reliable and flexible functions are performed by the versatile NMAT column. The NMAT head is the most sensitive part of the UTM as it is capable of sensing high resolution displacements as well as the ability to impart a small force on the NMAT column through electromagnetic actuation. The NMAT housing has a NMAT column that is attached to a center plate. The center plate is housed between a set of four charged capacitor plates (Figure 2.5). The up and down movement of the center plate causes the movement of the NMAT column. The NMAT column has a maximum displacement range of approximately 750 μm with a displacement resolution of less than 1 nm.

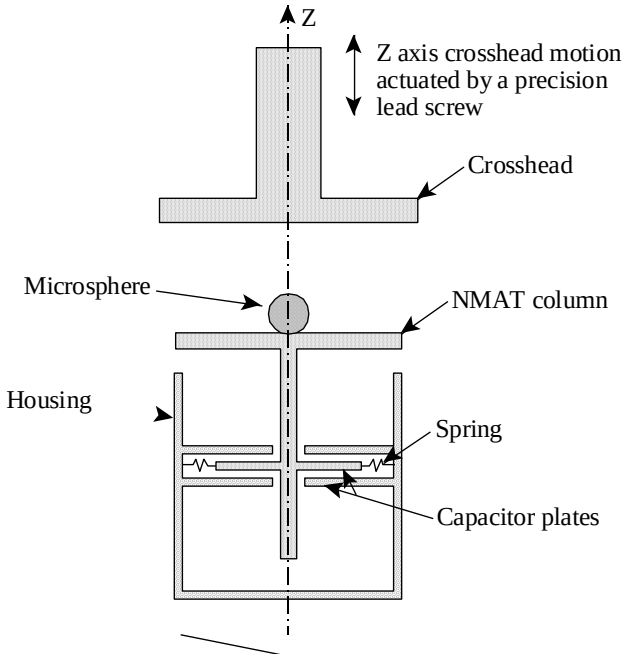

Figure 2.4: Schematic of the functional elements of the Nano-Bionix Universal Testing Machine [76].

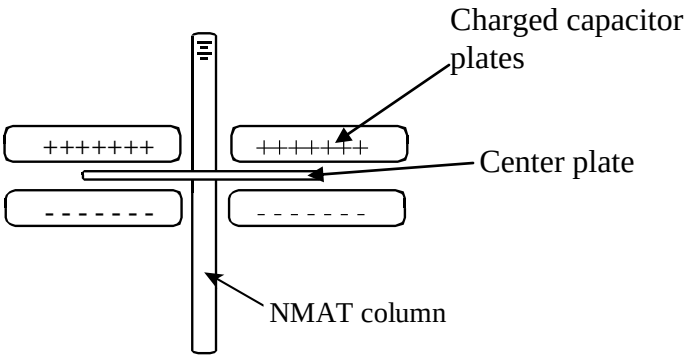

Figure 2.5: Schematic of the key components of the NMAT head [76].

The maximum load applied by the NMAT head is 500 mN with a force resolution of 50 nN. During operation, the computer continuously records the elapsed time, crosshead position, and raw electromechanical force on the NMAT column, raw position of the NMAT column, effective spring stiffness, and slope of the raw electromechanical

force signal versus the raw NMAT column position signal. This information can then be downloaded into a text file for post-processing and analysis.

The mechanical strength of the as-prepared CaLB3-40-S50 microspheres was tested by writing a stepwise program in the Test Works 4.0®. The following steps list the procedure for operation:

Step 1: A single microsphere was placed on the compression platen (1" diameter and 0.5" thick) screwed to the NMAT column.

Step 2: The crosshead was moved downward to make sure that it did not touch the microsphere but was positioned as close as possible to the microsphere.

Step 3: The crosshead was then moved toward the microsphere at 1 µm/s until the NMAT head was negatively displaced (displaced downward) by 1 µm. This was done to have coarse contact with the microsphere.

Step 4: The crosshead was then raised 16 µm to separate the surface of the microsphere and the crosshead.

Fine Approach and Contact

Step 5: The NMAT column was moved in the unloading direction toward the crosshead at 50 nm/s. The slope of NMAT column displacement versus raw electromechanical force was recorded. Intimate contact was assumed to be achieved between the microsphere and the NMAT column when the slope reached a threshold value of 250 N/m. At this point, the compressive load began acting on the microsphere and the crushing load exerted by the NMAT column increased at 2 mN/s.

Step 6: The rupturing force increased until the raw force showed an instantaneous drop indicating the rupture of the microsphere [76].

After writing down the stepwise procedure, the test was run by opening the test window (Figure 2.6). Parameters such as raw displacement (NMAT column displacement), raw load, center plate position, and the load versus displacement slope were recorded. As the test started, a real time graph showing variation of raw load (Figure 2.7) was recorded.

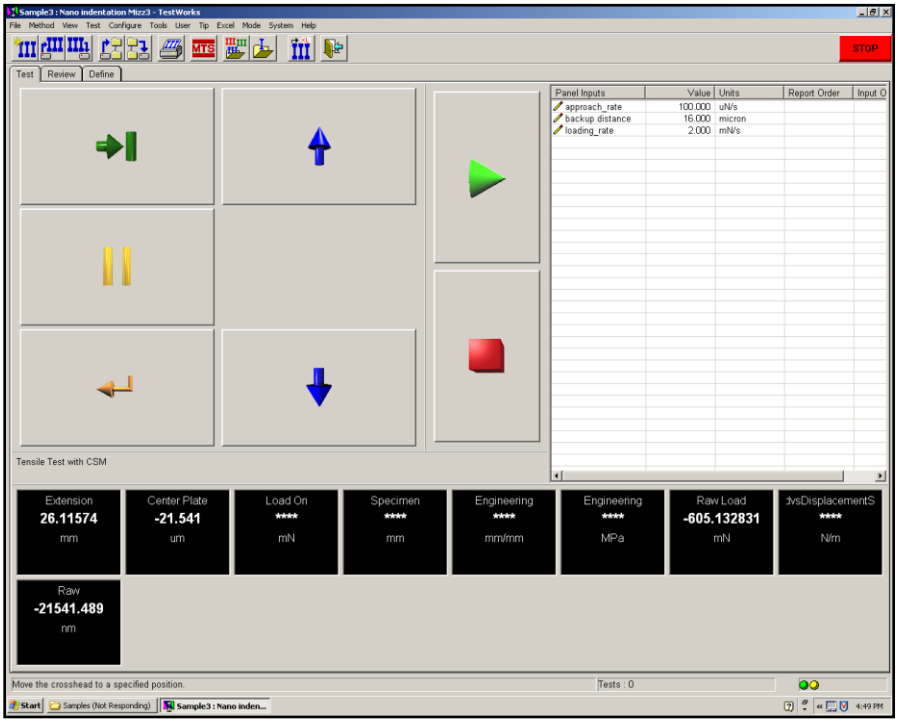

Figure 2.6: Test window showing various recorded parameters during operation.

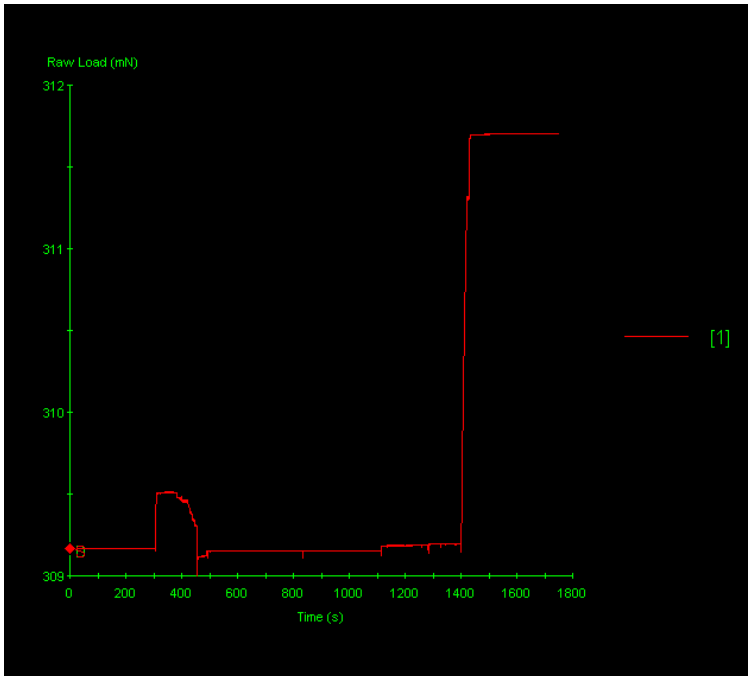

Figure 2.7: Variation of raw load with passage of time.

The following procedure describes the sequential movement of the NMAT column with reference to Figure 2.8.

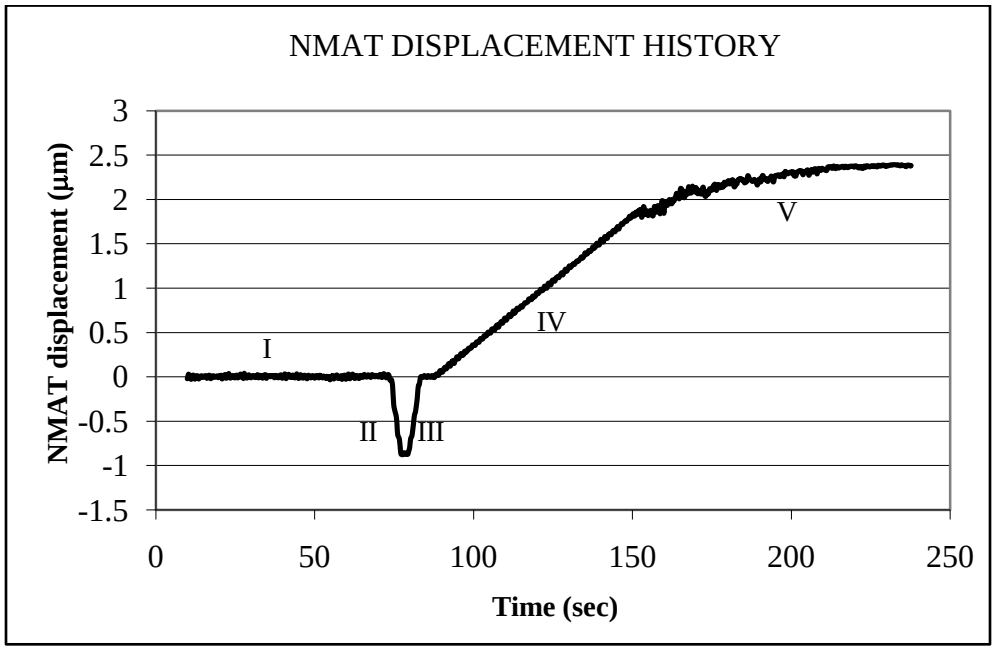

Figure 2.8: Typical NMAT column displacement graph [76].

I – The crosshead approached the NMAT column at 1 µm/s. During this time, the NMAT column was at its zero reference position.

II – The crosshead had coarse contact with the microsphere and kept displacing the NMAT column until it was displaced by 1 µm in the negative direction.

III – After the coarse contact was made, the crosshead was retracted by a distance of 16 µm. Also, the NMAT column followed the crosshead to its original reference position.

IV – The NMAT column began approaching the crosshead at 50 nm/s.

V – As soon as the NMAT column started making a fine contact with the asperities on the surface of the microsphere, the curve became discontinuous. The tips of the asperities started breaking apart as the contact increased between the NMAT column and microsphere. The contact stiffness i.e. slope of the raw force/NMAT displacement graph kept on varying between ± 100 N/m due to unavoidable background noise. The crushing of the microsphere began when the contact stiffness reached a threshold value of 250 N/m.

CaLB3-40-S50 reacted microspheres (+150/-355µm) were tested on the Nano-Bionix UTM to calculate the rupture force. The maximum nominal load applied by the UTM was approximately 500 mN, and hence the as-reacted microspheres did not show a decrease in load when tested on the UTM even after reaching the capacity load. Henceforth, as-prepared CaLB3-40-S50 and heat-treated reacted microspheres (heat-treated for 1 hour at 600ºC, 900ºC, and 1200ºC) were tested for their mechanical strength at Mo-Sci Corporation, Rolla, MO. An Instron testing machine having a ± 50 N static

load cell (Figure 2.9) was used to test the rupture strength of the as-prepared CaLB3-40-S50 microspheres and heat-treated CaLB3-40-S50 reacted microspheres.

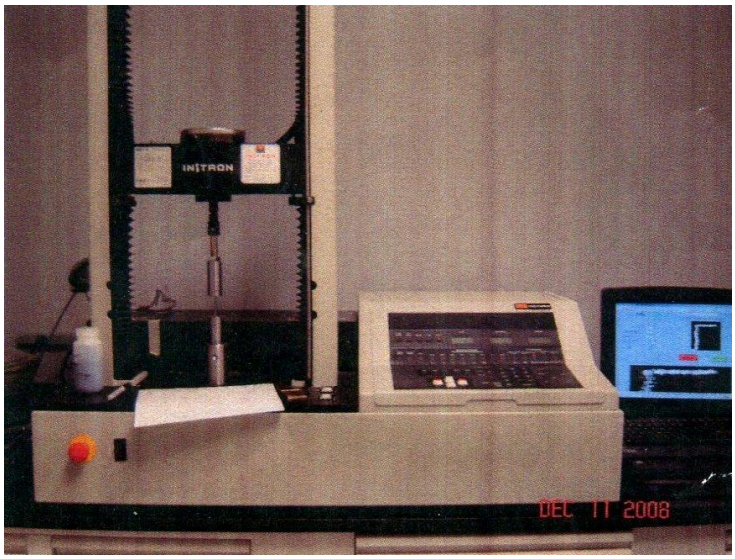

Figure 2.9: Instron machine used to measure mechanical strength of microspheres.

A single microsphere was first placed under a Keyence® optical microscope on a flat surface of the stainless steel anvil to measure the diameter of the microsphere. The stainless steel anvil (Figure 2.10) was placed in the Instron press and unidirectional compression was applied to the microsphere through the force rod (Figure 2.10) with a crosshead speed of 0.02 mm/min. Microscopic images were taken of the same microsphere after testing to determine whether it had ruptured. The diameters of the microspheres were measured to determine the crushing force as a function of particle diameter. The extension of the force rod was recorded and later used to calculate the contact area at the rupture point of the microspheres.

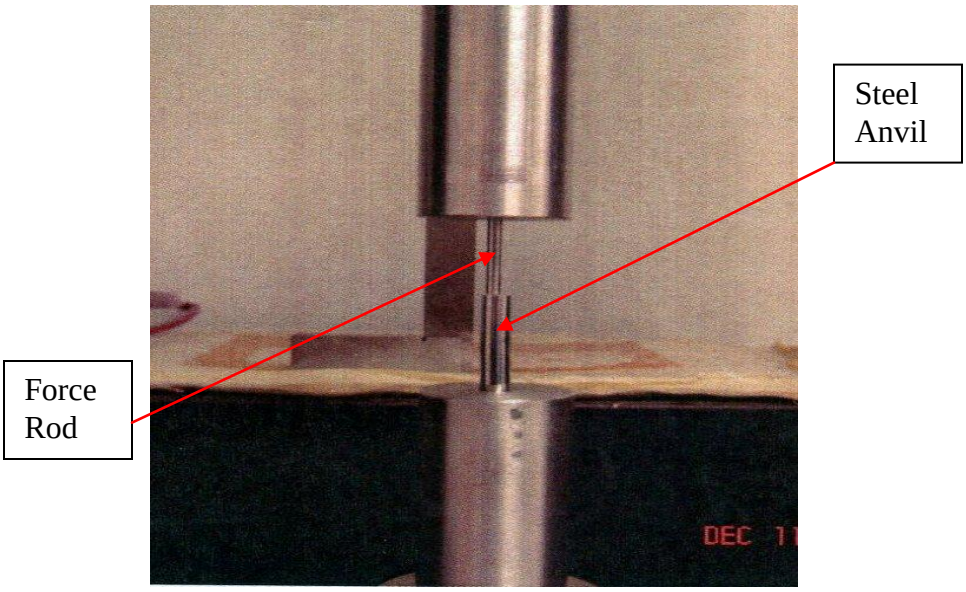

Figure 2.10: Steel anvil (on which microsphere was placed) and force rod (through which force was applied to the microsphere).

3. RESULTS AND DISCUSSIONS

3.1. CONVERSION OF CaLB3 MICROSPHERES

3.1.1. Comparison of CaLB3-20-MoSci Glass Microspheres with CaLB3-20-Fears Glass Microspheres.

CaLB3-20-MoSci glass microspheres were reacted at 37°C in 0.25 M K_2HPO_4 solution at pH = 9 (± 0.05) for 2 days, and results were qualitatively compared with those obtained by Fears [51] for his self-prepared CaLB3-20 microspheres. CaLB3-20-MoSci glass particles formed hollow microspheres after non-uniform reaction, which was in conformance with Fears's results that CaO ≤ 20 wt% yields hollow microspheres [51]. Figure 3.1 shows the hollow microstructures for reacted CaLB3-20-MoSci microspheres and Figure 3.2 shows hollow CaLB3-20-Fears microspheres. Hence it was concluded that CaLB3-20 glass microspheres yielded hollow microspheres irrespective of the source of preparation.

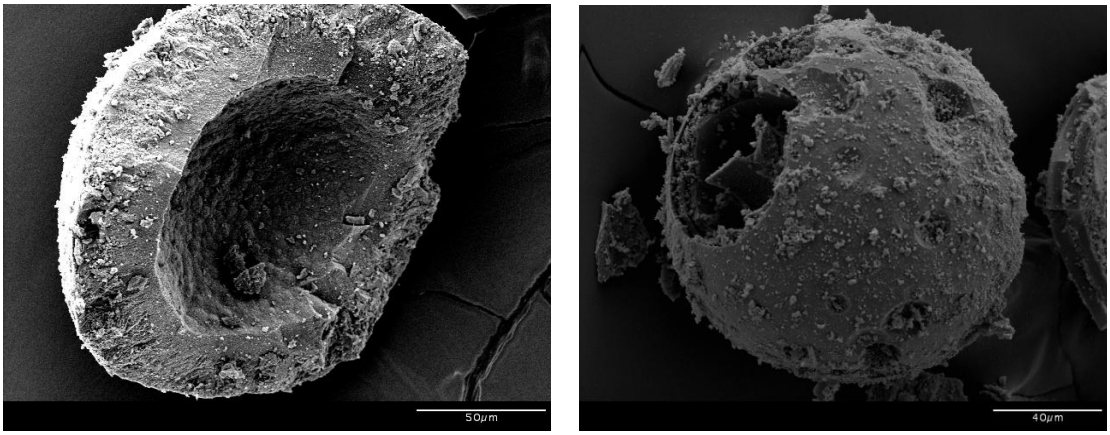

Figure 3.1: Reacted hollow microstructure of CaLB3-20-MoSci microspheres (0.25 M K_2HPO_4, pH=9, 37˚C, 2 days).

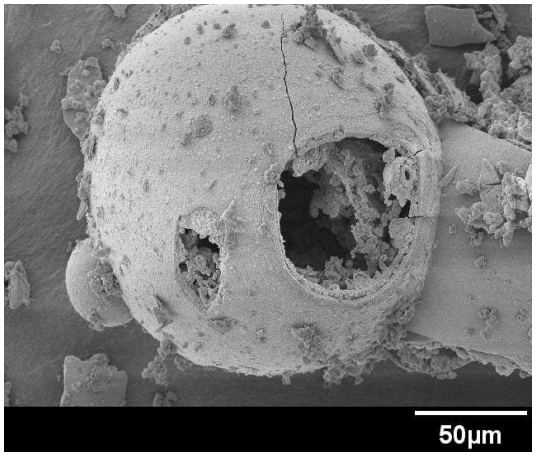

Figure 3.2: Reacted hollow microstructure of CaLB3-20-Fears microsphere (0.25 M K_2HPO_4, pH=9, 37˚C, 2 days). [51]

After reaction, the external surface of the reacted microspheres exhibited needle-like particles (Figure 3.3), which are characteristic of microstructure present in natural bone [1]. However, the internal microstructure of the reacted microspheres varied from the surface, as shown in Figure 3.4. The reacted CaLB3-20-MoSci microspheres had a closely packed dense layer approximately 1.5-2.0 µm thick consisting of needle-like HAp particles (Figure 3.4). As Ca-P precipitate starts forming from surface towards the center of the microsphere, the preceding reacted layers start consolidating to form a dense HAp layer with reduced porosity. This dense layer is prominent in CaLB3-20 microspheres due to low CaO content.

In order to look at the cross-section of the reacted CaLB3-20-MoSci microspheres, mechanically polished epoxy embedded samples were observed with SEM. The reacted layer was approximately 16-20 µm thick (Figure 3.5) for a microsphere approximately 100 µm in diameter. The average value of thickness was based on readings for 3-4 microspheres with five readings for each microsphere. The hollow volume percentage in the reacted microspheres was measured to be approximately 44%. This implies that CaLB3-20-MoSci microspheres were converted into hollow HAp

microspheres consisting of a dense layer of HAp on the periphery. This dense layer was not present in glass microspheres with higher CaO content (as discussed in proceeding sections).

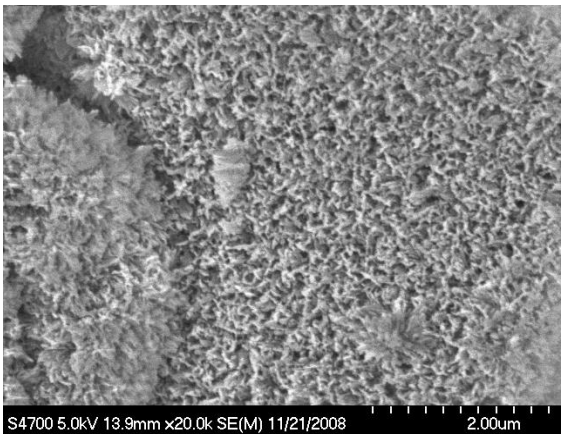

Figure 3.3: Grain-like surface microstructure of the reacted microspheres (0.25 M K_2HPO_4, pH=9, 37˚C, 2 days).

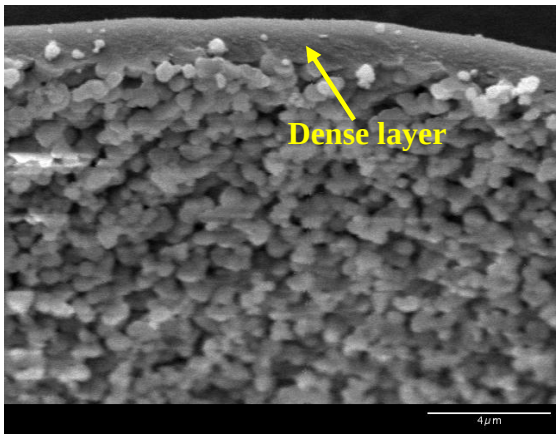

Figure 3.4: Closely packed dense layer of HAp particles (0.25 M K_2HPO_4, pH=9, 37˚C, 2 days).

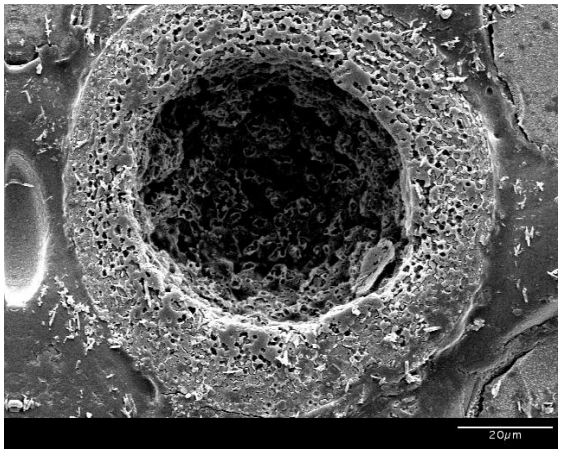

Figure 3.5: Cross-section of polished reacted CaLB3-20-MoSci microsphere (0.25 M K_2HPO_4, pH=9, 37˚C, 2 days).

3.1.2. Comparison of CaLB3-40-Fears Glass Microspheres with CaLB3-20 Fears Glass Microspheres and Validation of Fears's Results. CaLB3-40-Fears glass microspheres were reacted in a 0.25 M K_2HPO_4 solution at pH = 12 (± 0.05) at 37ºC for 2 days. The results were analyzed to validate Fears's conclusion according to which CaO ≥ 40 wt% yielded solid but porous microspheres. The SEM analysis of the partially reacted CaLB3-40-Fears microspheres revealed signs of conversion to amorphous calcium phosphate by presence of reacted shells (confirmed by X-ray mapping) which came off the unreacted core once the partially reacted microspheres were fractured (Figure 3.6).

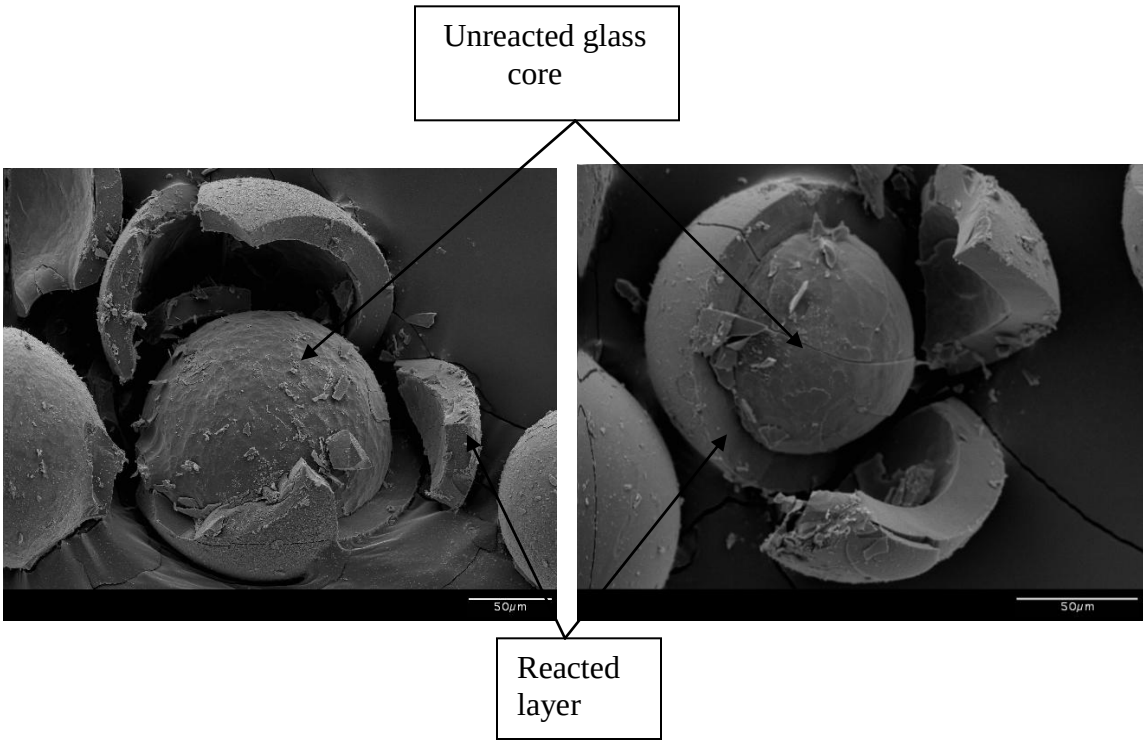

Figure 3.6: SEM images of partially reacted CaLB3-40-Fears microspheres (0.25 M K_2HPO_4, pH=12, 37˚C, 2 days).

For the same number of days (2 days); CaLB3-20-Fears microspheres had converted to hollow microshells whereas CaLB3-40 microspheres still had unreacted

glass cores intact. In order to look at the cross-section of the reacted CaLB3-40-Fears microspheres, mechanically polished epoxy embedded samples were observed under SEM. The reacted layer was approximately 26-30 µm thick (Figure 3.7) for a microsphere approximately 100 µm in diameter. The average value of thickness was based on readings for 3 to 4 microspheres with five readings for each microsphere. There was an increase in the thickness of the reacted layer by 55% as compared to reacted CaLB3-20-Fears microspheres which shows that calcium content has an effect on the thickness of the reacted layer.

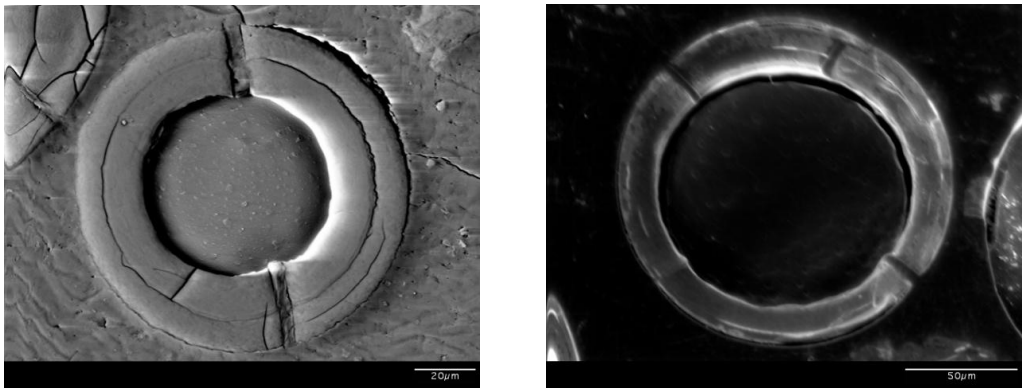

Figure 3.7: Cross-section of partially reacted CaLB3-40-Fears microspheres (0.25 M K_2HPO_4, pH=12, 37˚C, 2 days).

X-ray mapping confirmed the formation of a calcium-phosphorus precipitate (Ca-P) layer surrounding the unreacted glass core at the center. EDS analysis for the polished particles showed presence of phosphorus peaks in the reacted layer. EDS analysis of the reacted layer gave a Ca/P atomic ratio of approximately 1.44, which implies that calcium deficient HAp was formed. Generally, HAp formed by precipitation reactions is calcium deficient and has poor crystallinity [48]. Figure 3.8 shows the X-ray maps and Figures

3.9 and 3.10 show EDS analyses for the cross sections of reacted CaLB3-40-Fears microspheres respectively. Hence, CaLB3-40-Fears glass microspheres began transforming into solid but porous calcium deficient HAp microspheres. However, a dense layer of HAp was missing in these partially reacted microspheres.

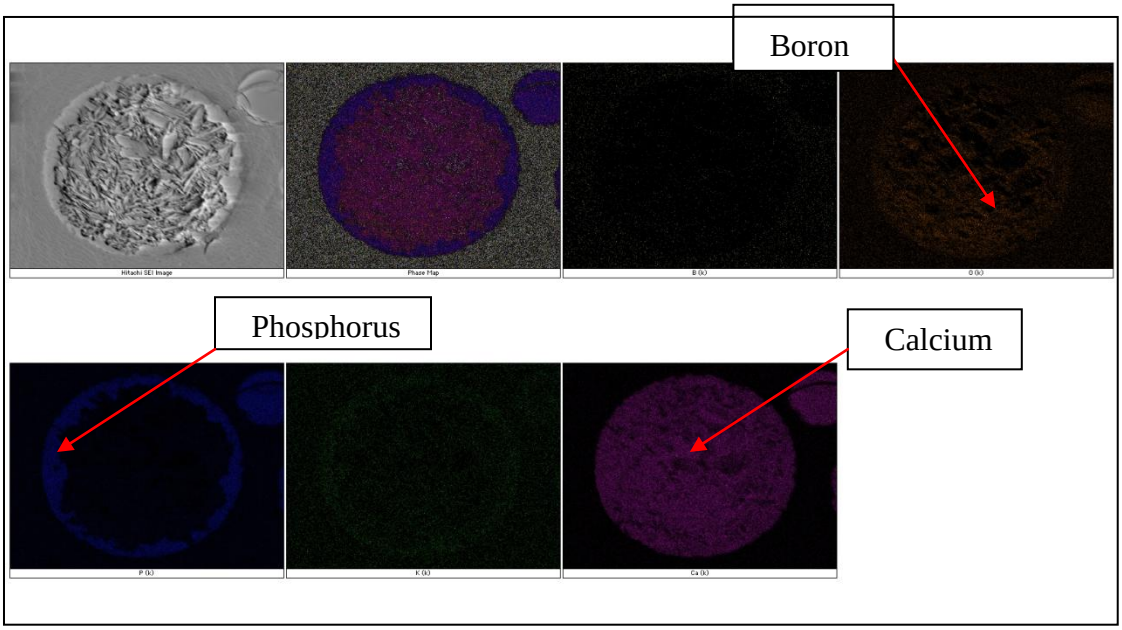

Figure 3.8: X-ray maps for partially reacted CaLB3-40-Fears microspheres (0.25 M K_2HPO_4, pH=12, 37˚C, 2 days) showing presence of calcium, phosphorus, and boron.

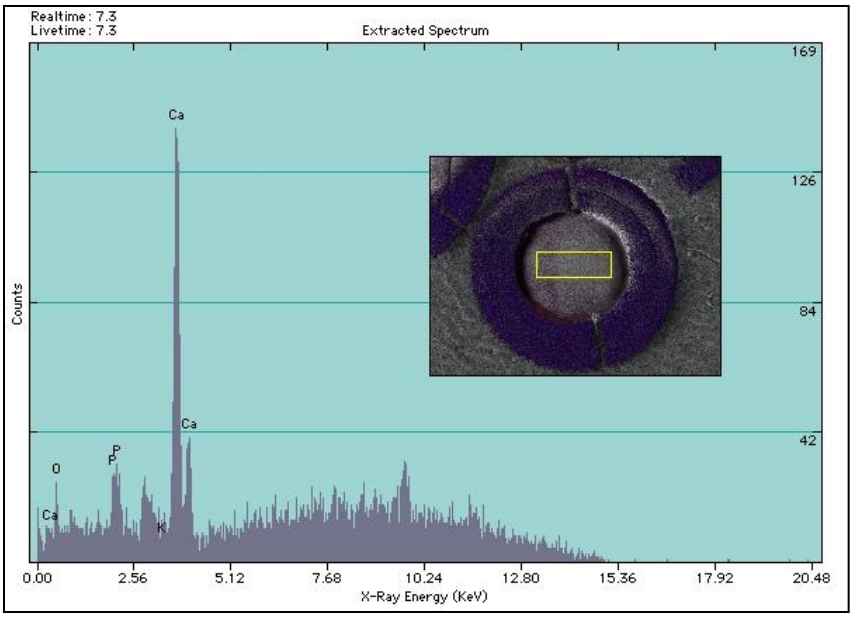

Figure 3.9: EDS analysis for partially reacted CaLB3-40-Fears microspheres (0.25 M K_2HPO_4, pH=12, 37˚C, 2 days) showing presence of major calcium peak.

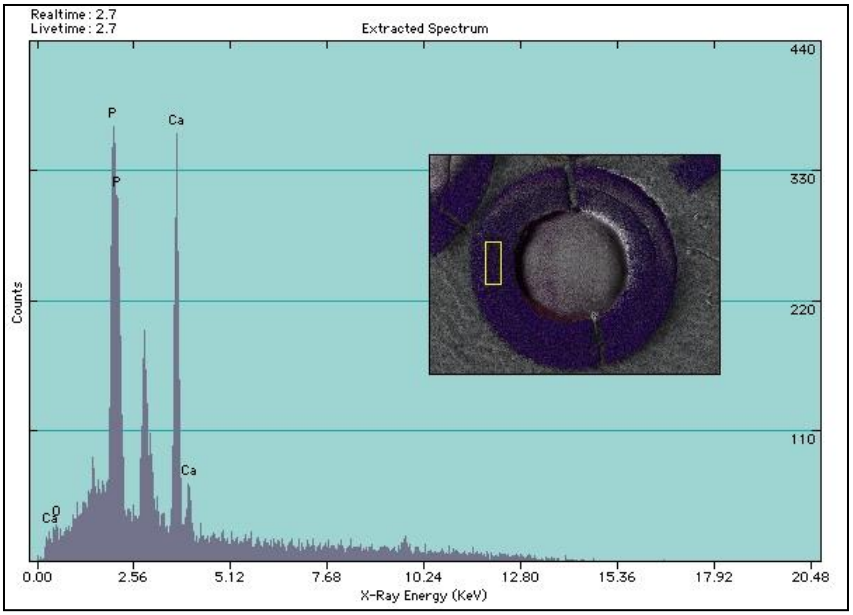

Figure 3.10: EDS analysis for partially reacted CaLB3-40-Fears microspheres. It shows presence of major calcium and phosphorus peaks in the reacted layer confirming the formation of an amorphous calcium phosphate layer which later recrystallizes into calcium deficient HAp.

3.1.3. Comparison of CaLB3-40-MoSci Glass Microspheres with CaLB3-20-MoSci Glass Microspheres. Conversion of CaLB3-40-Fears microspheres validated the conclusions proposed by Fears of formation of solid but porous microspheres. The main emphasis of this research was to convert CaLB3-40 microspheres to HAp and characterize them. The advantage of the CaLB3-40 glass microspheres is that they are quite mechanically strong as compared to the hollow microshells yielded by conversion of CaLB3-20 glass microspheres. Furthermore, CaLB3-40-MoSci glass microspheres were reacted as per the conditions mentioned in the experimental procedure. Figure 3.11 confirmed unreacted glass core at the center whereas CaLB3-20-MoSci converted to hollow microshells for the same number of days of reaction. Also, the surface of the reacted microspheres had a needle-like microstructure similar to that of natural bone. Hence, glass microspheres from Mo-Sci Corporation (with different compositions) also reacted in the same way as proposed by Fears.

Figure 3.11: SEM image of partially reacted CaLB3-40-MoSci microsphere (0.25 M K_2HPO_4, pH=12, 37˚C, 2 days).

3.1.4. Problem with Conversion of CaLB3-40-MoSci Glass Microspheres. SEM microstructural analysis of reacted CaLB3-40-MoSci microspheres revealed no promising signs of conversion to HAp even at longer durations of reaction at higher concentrations and at higher temperatures. Figure 3.12 (a) shows the cut section of a deliberately broken partially reacted CaLB3-40-MoSci glass microsphere. Figure 3.12 (b) showed that the reacted layer was only about 3 µm thick even after reaction at 0.5 M concentration and 70^{o}C reaction temperature. Figure 3.13 shows the reacted layer consisting of a grain-like microstructure. The reacted layer was confirmed by X-ray mapping (Figure 3.14). The duration of reaction was increased up to 4 days and 10 days but nothing significant was achieved. The XRD pattern (Figure 3.15) for the reacted CaLB3-40-MoSci microspheres finally confirmed that they did not convert to HAp. The following SEM images show the reaction extent for the listed conditions:

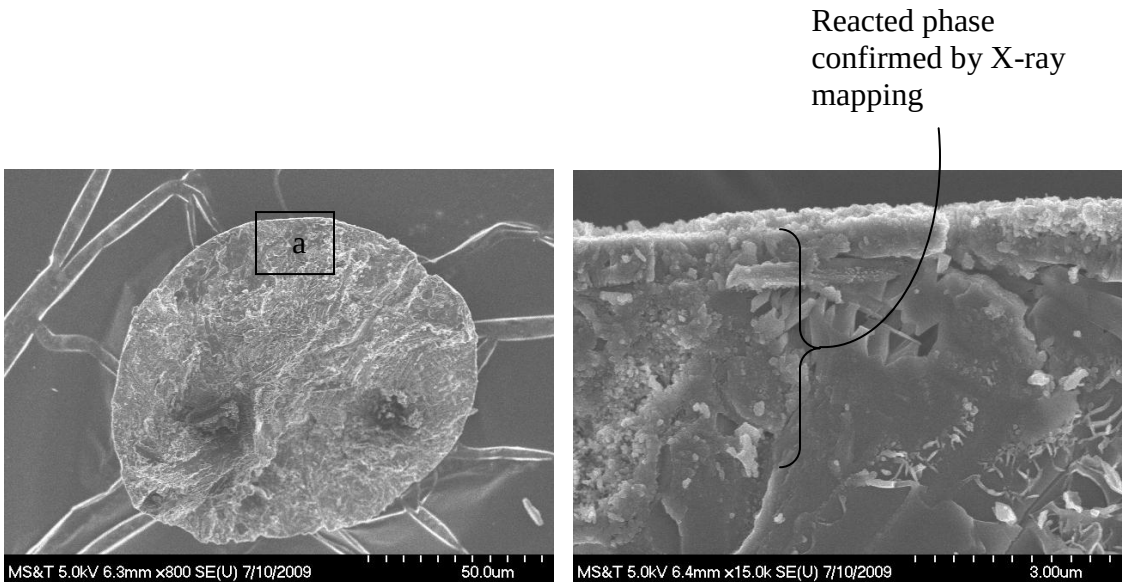

(a) (b)

Figure 3.12: (a) SEM images of CaLB3-40-MoSci microspheres reacted at 70°C in 0.5 M phosphate solution (pH=12) for 2 days. (b) Magnified image of area (a).

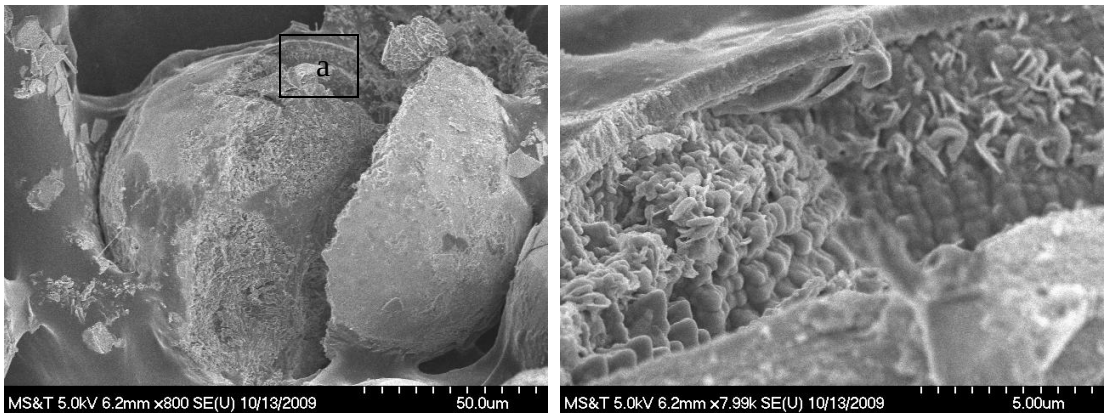

(a) (b)

Figure 3.13: (a) SEM images of CaLB3-40-MoSci microspheres reacted at 70°C in 0.5 M phosphate solution (pH=12) for 4 days. (b) Magnified image of area (a). The reacted layer is approximately 5 μm thick.

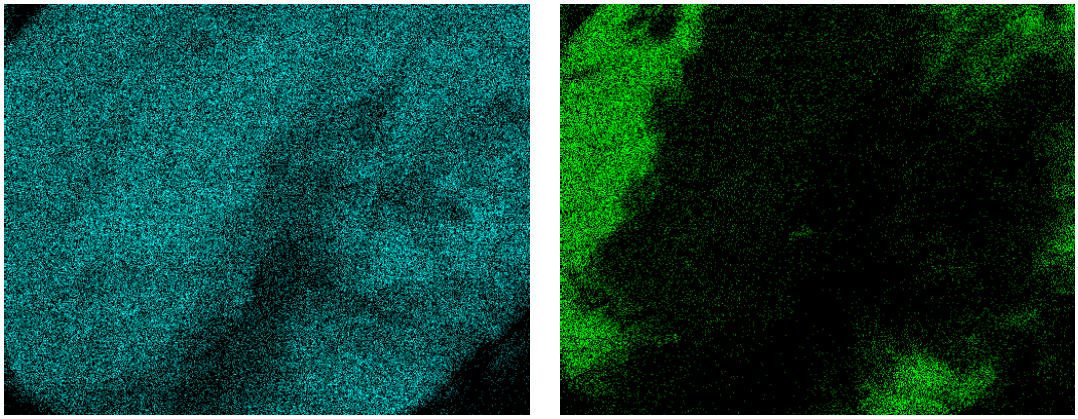

(a) (b)

Figure 3.14: X-ray map of area in Figure 25(a) showing presence of (a) calcium throughout the microstructure, and (b) phosphorus on the periphery.

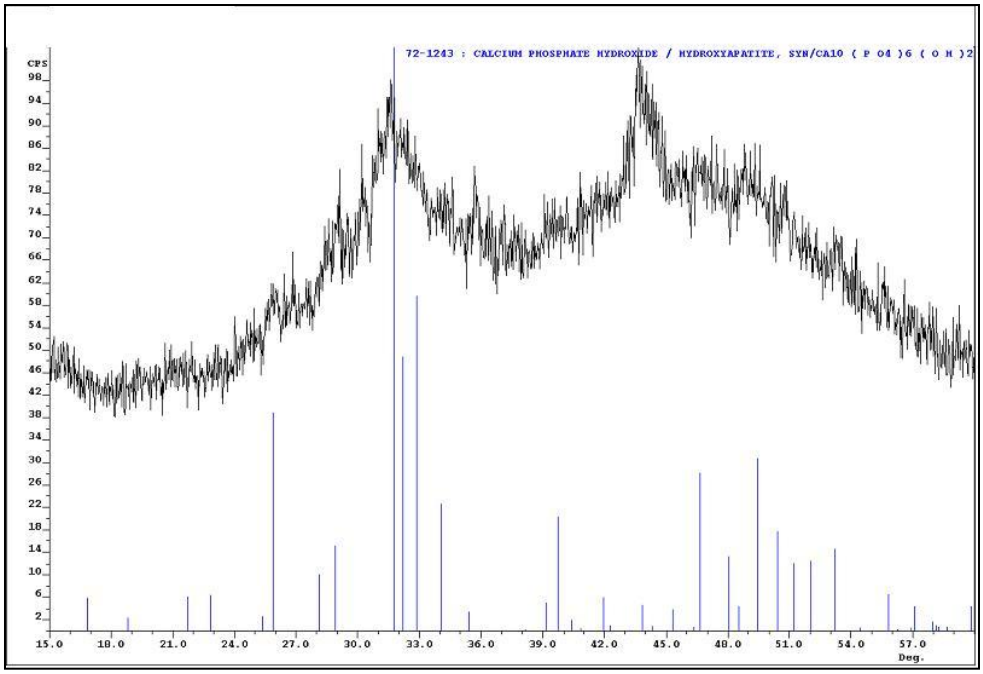

Figure 3.15: XRD pattern showing crystal structure of reacted CaLB3-40-MoSci microspheres (at 70˚C in 0.5 M phosphate solution for 4 days) with commercial HAp pattern overlaid.

The CaLB3-40-MoSci glass microspheres were spheridized using a propane torch flame whereas CaLB3-40-Fears glass microspheres were spheridized using a drop tube furnace. The difference in the spheridization technique was supposed to be the reason for the variation in reaction product. A propane torch flame was assumed to be the reason for creating high levels of crystallinity in glass microspheres but this reason was not very concrete to attribute to the failure of conversion of CaLB3-40-MoSci glass microspheres. Henceforth, CaLB3-40 glass frit was obtained from Mo-Sci Corporation and spheridized in the drop tube furnace. The resultant glass microspheres were reacted in 0.5 M phosphate solution at 37˚C (pH = 10) for 16 days. SEM analysis still did not show complete conversion of the particles. Finally it was concluded that CaLB3-40-MoSci glass microspheres would take up to 10 weeks for complete conversion. Ultimately, CaLB3-40-SX glass microspheres were prepared and reacted.

3.1.5. Conversion of CaLB3-40-SX Glass Microspheres.

3.1.5.1. Emphasis on CaLB3-40-S50 and CaL3-40-S75 Glass Microspheres.

The main emphasis was on reacting CaLB3-40-S50 and CaLB3-40-S75 glass microspheres as they were completely amorphous in form when prepared. The level of crystallinity was the highest for CaLB3-40-S100 glass microspheres and could be due to the huge amount of trapped SO_2 gas trapped inside glass network that is formed by the decomposition of $CaSO_4$. In order to elucidate the effect of sulfur on the conversion rates, CaLB3-40-S25 through CaLB3-40-S100 glass microspheres were reacted in 1 M phosphate solution at 37˚C (pH = 10) for 6 days. The XRD pattern showed that CaLB3-40-S75 glass microspheres were completely converted to HAp microspheres in 6 days (Figure 3.16).

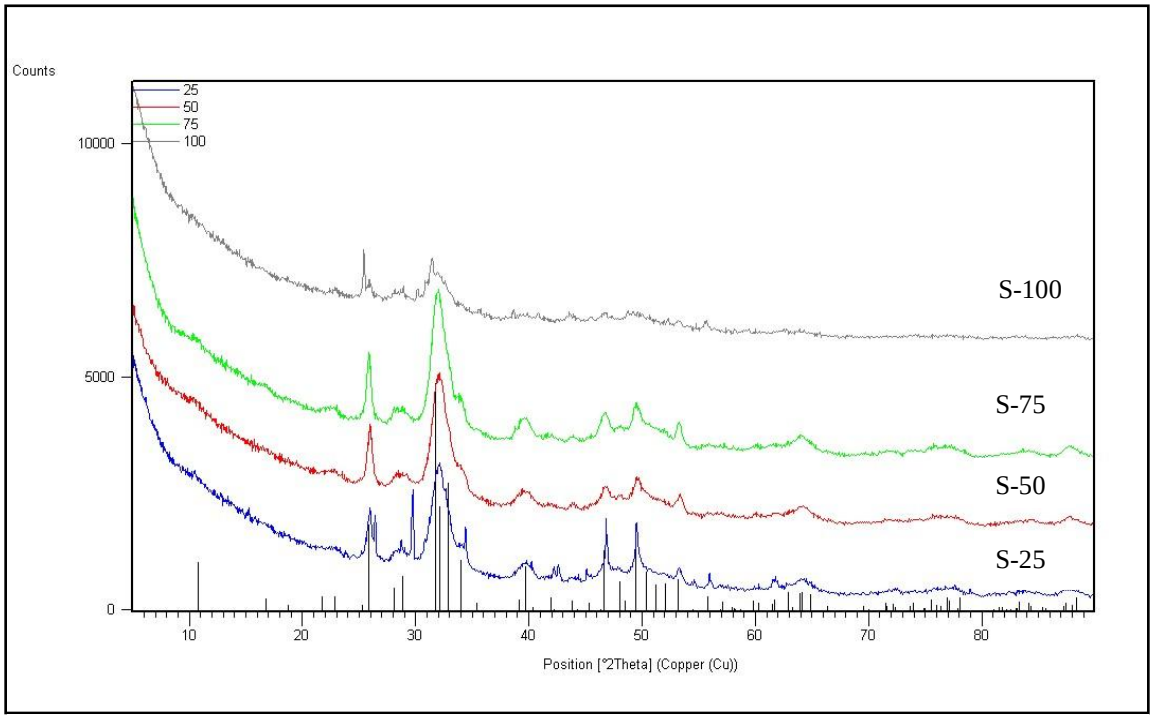

Figure 3.16: XRD patterns for reacted CaLB3-40-S25 through CaLB3-40-S100 glass microspheres reacted in 1.0 M phosphate solution; pH=10; 37˚C; 6 days.

The XRD pattern for reacted CaLB3-40-S25 glass microspheres contained some peaks corresponding to calcium borate. Also, reacted CaLB3-40-S100 glass microspheres consisted of crystalline $CaSO_4$ peaks. Hence, further characterization was done for CaLB3-40-S50 and CaLB3-40-S75 glass microspheres.

3.1.5.2. CaLB3-40-S50 glass microspheres.

3.1.5.2.1. SEM characterization and effect of concentration of phosphate solution. CaLB3-40-S50 glass microspheres were reacted at 37°C in K_2HPO_4 solution (pH=12 ± 0.05) at 0.25 M, 0.50 M, 0.75 M, 1.00 M, and 1.50 M concentrations for 6 days and 12 days at each concentration level. The walls of the partially reacted microspheres were examined by SEM and showed signs of layer by layer reaction (Figure 3.17). The reason for this surface layer formation is compositional variability of HAp which ranges from stoichiometric HAp (Ca/P = 1.66) to fully calcium-deficient HAp [77]. The composition of the surface layers is generally different from the bulk composition.

The morphology of the partially reacted CaLB3-40-S50 microspheres confirmed the formation of various phases during dissolution of glass microspheres (Figure 3.18). Literature review shows that initially, an unstable phase of amorphous calcium phosphate (ACP) is formed which transforms to amorphous calcium-deficient HAp and further changes to crystalline calcium-deficient HAp. The transformation of ACP to HAp continues until all the calcium in the glass network is consumed [77]. HAp starts forming on the surface and continues crystallizing on the inner wall as shown in Figure 3.18. CaLB3-40-S50 glass microspheres reacted in the same way as the CaLB3-40-Fears glass microspheres. The partially reacted microspheres still had an unreacted glass core intact

at the center but the reacted layer was much thicker than partially reacted CaLB3-40-MoSci glass microspheres.

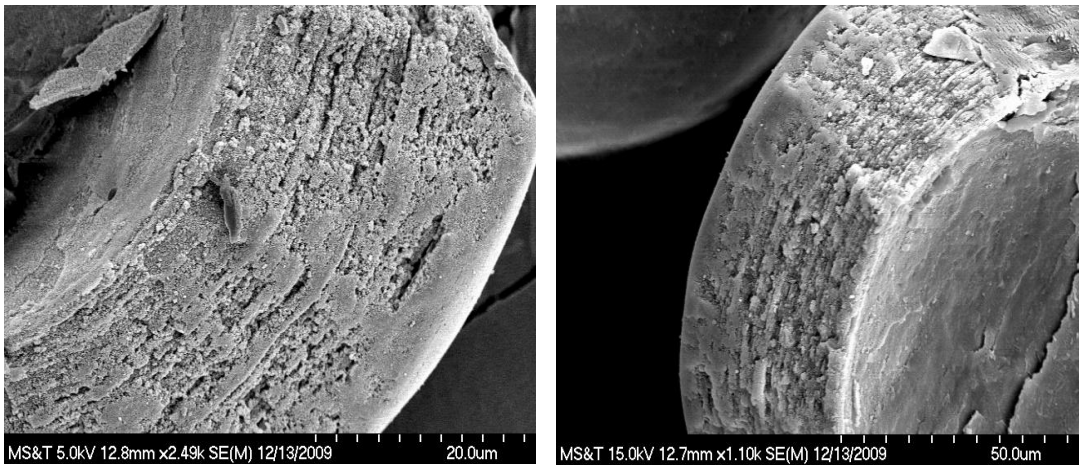

Figure 3.17: SEM images of the wall of partially reacted CaLB3-40-S50 microsphere in 0.5 M phosphate solution (pH=10) at 37˚C for 2 days showing layer by layer reaction.

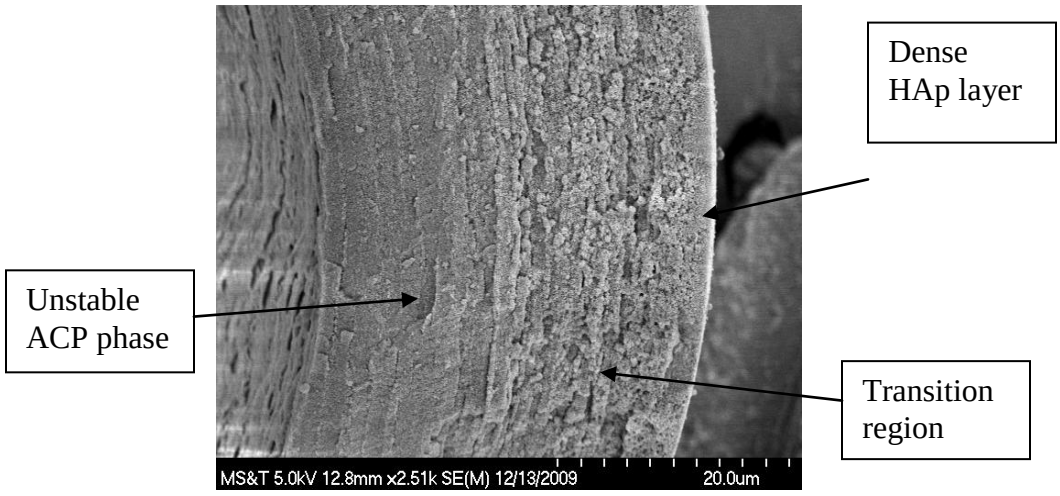

Figure 3.18: SEM image of the wall of partially reacted CaLB3-40-S50 microsphere in 0.5 M phosphate solution (pH=10) at 37˚C for 2 days.

The reacted CaLB3-40-S50 glass microspheres under different conditions were analyzed for the reacted layers. The thickness of the reacted layers was calculated using Image J software. The average value of thickness was based on readings for 5

microspheres with five readings for each microsphere. The d/D ratios were calculated where,

d = 2 * thickness measured by Image J software and

D = Diameter of the microsphere.

The following SEM images (Figure 3.19 through Figure 3.23) show the reacted layer for different concentrations. Table 3.1 lists the d/D values for the reacted microspheres. The SEM images and the measured d/D ratios revealed that the microspheres were completely reacted within 6 days at 1.5 M concentration and 12 days at 1.0 M concentration. Small voids were evident in the cross sections of the fractured reacted microspheres in some cases due to a gas bubble trapped inside the initial glass.

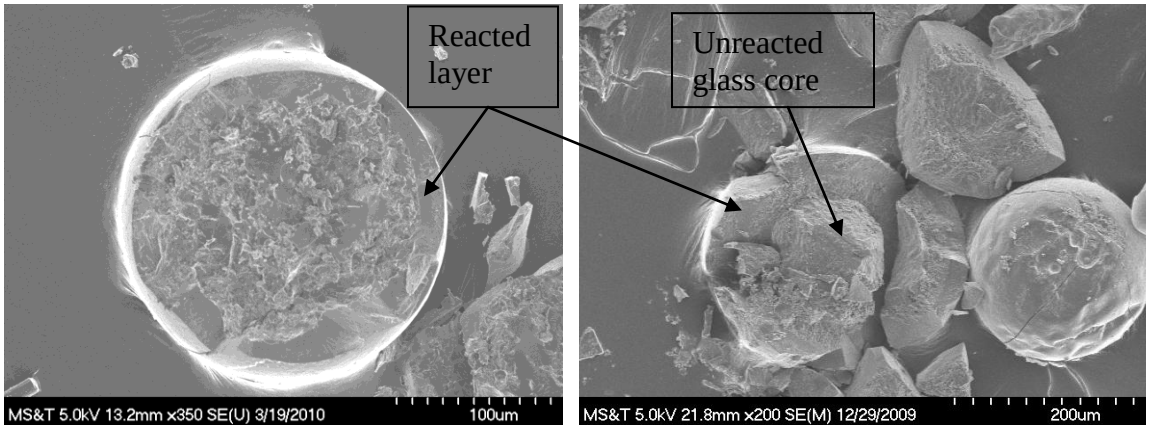

(a) (b)

Figure 3.19: SEM images of CaLB3-40-S50 microspheres reacted at 37°C in 0.25 M phosphate solution (pH=10) for (a) 6 days and (b) 12 days.

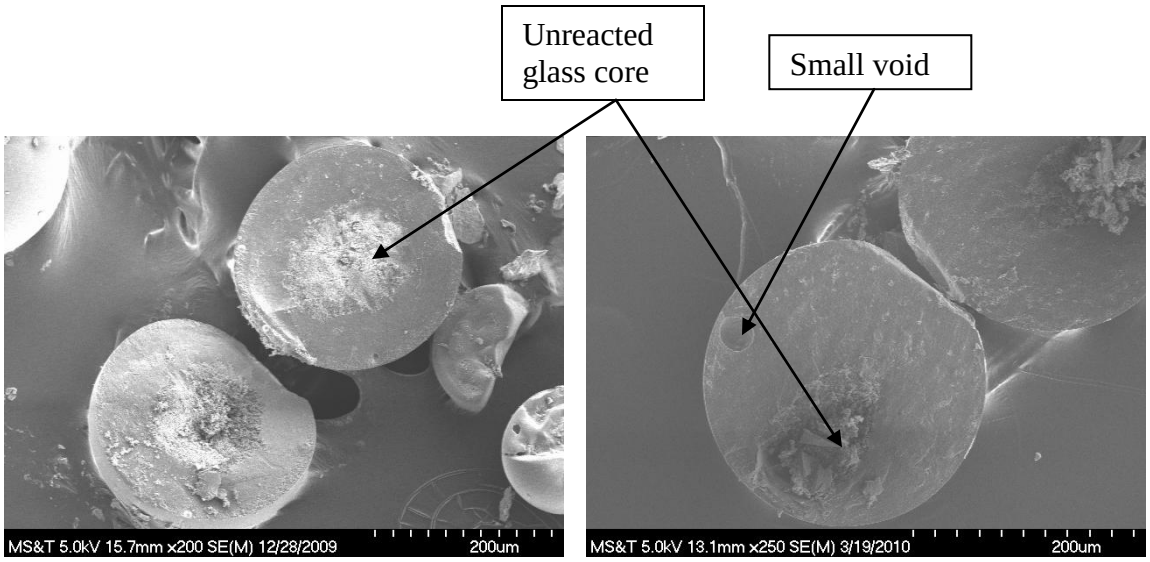

(a) (b)

Figure 3.20: SEM images of CaLB3-40-S50 microspheres reacted at 37°C in 0.50 M phosphate solution (pH=10) for (a) 6 days and (b) 12 days.

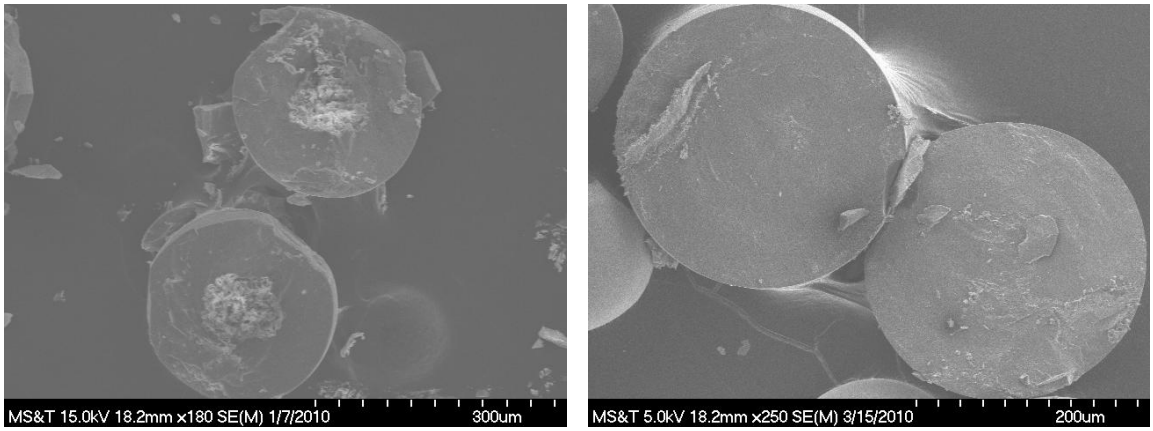

(a) (b)

Figure 3.21: SEM images of CaLB3-40-S50 microspheres reacted at 37°C in 0.75 M phosphate solution (pH=10) for (a) 6 days and (b) 12 days.

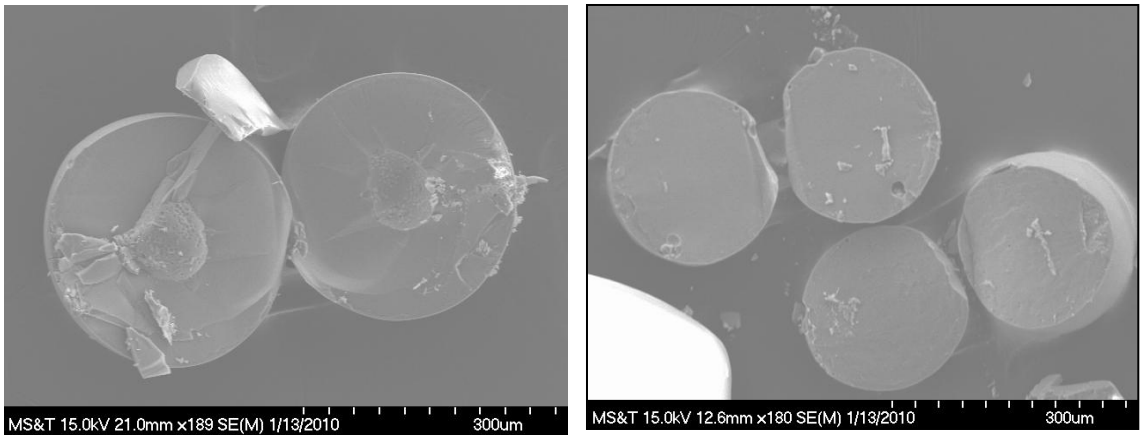

(a) (b)

Figure 3.22: SEM images of CaLB3-40-S50 microspheres reacted at 37°C in 1.00 M phosphate solution (pH=10) for (a) 6 days and (b) 12 days.

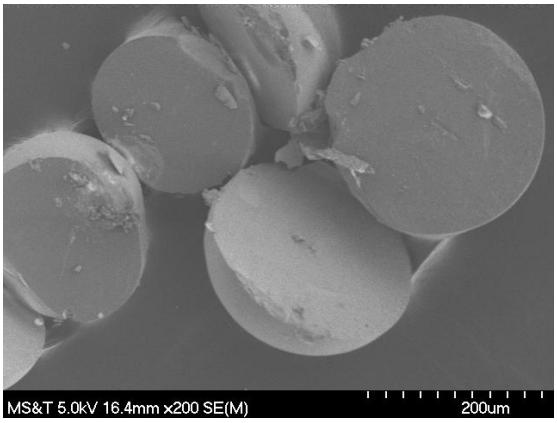

Figure 3.23: SEM image of CaLB3-40-S50 microspheres reacted at 37°C in 1.50 M phosphate solution (pH=10) for 6 days.

Table 3.1: Effect of concentration of phosphate solution on d/D ratio of reacted CaLB3-40-S50 microspheres.

Time / Concentration	6 days	12 days
0.25 M	0.16	0.21
0.50 M	0.58	0.64
0.75 M	0.78	~ 1.00
1.00 M	0.86	1.00
1.50 M	1.00	NA

3.1.5.2.2. <u>EDS characterization</u>. A standardless quantitative analysis was performed on reacted CaLB3-40-S50 microspheres to calculate the Ca to P molar ratio. The results confirmed the formation of calcium-deficient HAp. HAp compositions formed by precipitation from solution are generally calcium-deficient and have poor crystallinity [48]. The composition of stoichiometric HAp is $Ca_{10}(PO_4)_6OH_2$ with Ca/P = 1.67 whereas calcium-deficient HAp is denoted by $Ca_{(10-x)}(HPO_4)_x(PO_4)_{(6-x)}OH_{(2-x)}$ where x ranges from 0 to 1 [51]. There has been no limit on the Ca to P value as some literature describes the formation of calcium deficient HAp with Ca/P = 1.33 [77]. Figures 3.24 and 3.25 show the quantitative results that were used to calculate the Ca/P ratio.

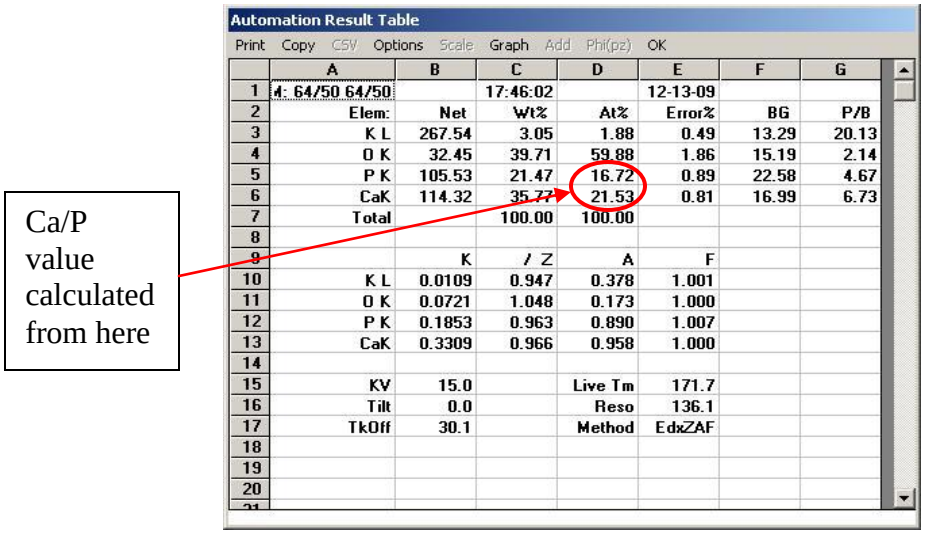

	A	B	C	D	E	F	G
1	4: 64/50 64/50		17:46:02		12-13-09		
2	Elem:	Net	Wt%	At%	Error%	BG	P/B
3	K L	267.54	3.05	1.88	0.49	13.29	20.13
4	O K	32.45	39.71	59.88	1.86	15.19	2.14
5	P K	105.53	21.47	16.72	0.89	22.58	4.67
6	CaK	114.32	35.77	21.53	0.81	16.99	6.73
7	Total		100.00	100.00			
8							
9		K	/ Z	A	F		
10	K L	0.0109	0.947	0.378	1.001		
11	O K	0.0721	1.048	0.173	1.000		
12	P K	0.1853	0.963	0.890	1.007		
13	CaK	0.3309	0.966	0.958	1.000		
14							
15	KV	15.0		Live Tm	171.7		
16	Tilt	0.0		Reso	136.1		
17	TkOff	30.1		Method	EdxZAF		
18							
19							
20							

Figure 3.24: Quantified results of standardless EDS analysis on S-4700 scope for reacted CaLB3-40-S50 microspheres showing atomic and weight percentages of constituent elements.

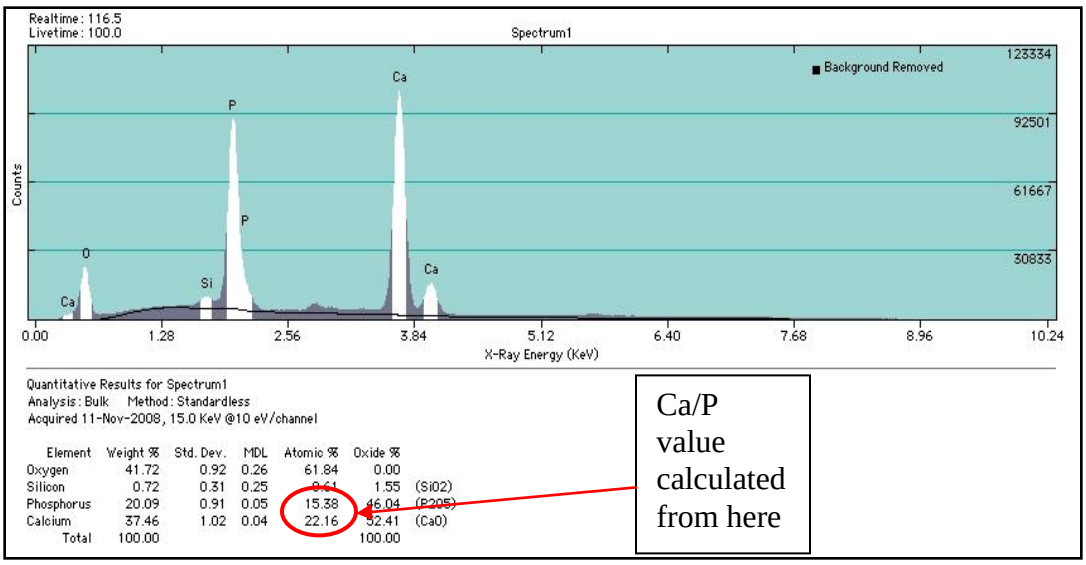

Figure 3.25: Quantified results of standardless EDS analysis on S-570 scope for reacted CaLB3-40-S50 microspheres showing atomic and weight percentages of constituent elements.

The following SEM images (Figure 3.26 and 3.27) show the Ca/P values for CaLB3-40-S50 glass micropsheres calculated by EDS analysis. The values of Ca/P varied over a range from 1.36 to 1.53. The unreacted glass core had a much higher Ca/P value as compared to the reacted shell.

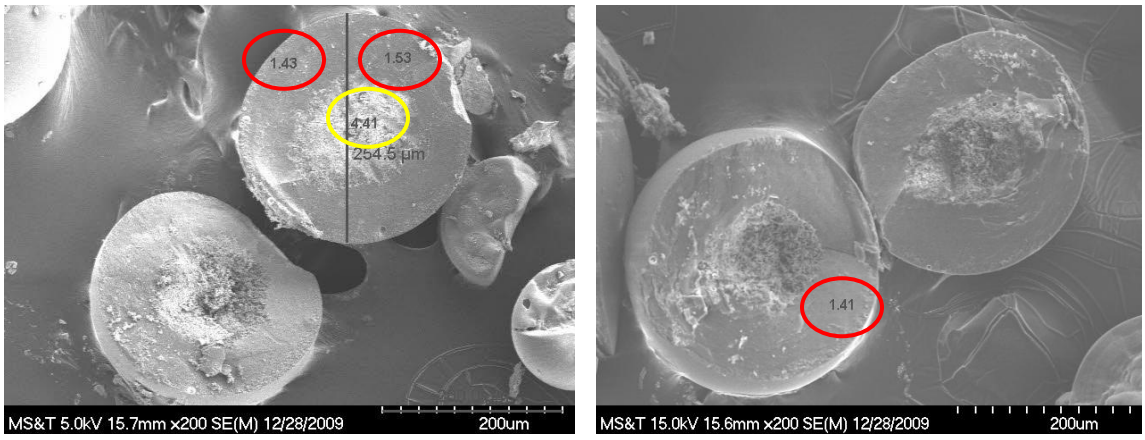

Figure 3.26: Partially reacted CaLB3-40-S50 microspheres in 0.5 M phosphate solution at 37°C for 6 days. The reacted shell has a Ca/P value of 1.43, 1.53, 1.41, and 1.36. The Ca/P value for the unreacted glass core is 4.41.

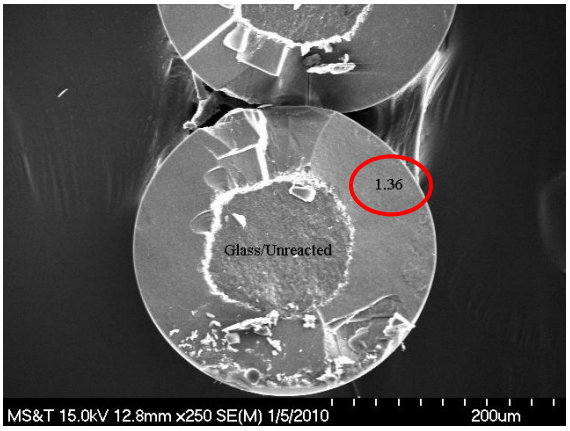

Figure 3.26: Partially reacted CaLB3-40-S50 microspheres in 0.5 M phosphate solution at 37°C for 6 days. The reacted shell has a Ca/P value of 1.43, 1.53, 1.41, and 1.36. The Ca/P value for the unreacted glass core is 4.41 (Contd.).

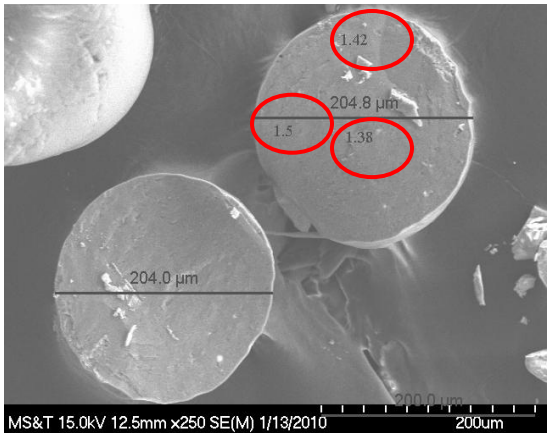

Figure 3.27: Completely reacted CaLB3-40-S50 microspheres in 1.0 M phosphate solution at 37°C for 12 days.

3.1.5.2.3. <u>X-ray mapping characterization</u>. Reacted CaLB3-40-S50 microspheres were analyzed by X-ray mapping to confirm the extent of reacted Ca-P layer (Figure 3.28). Colored X-ray maps were retrieved for the elements after the EDS analysis. The X-ray maps clearly showed that the unreacted glass core comprised of sulfur (Figure 3.29). As the reaction progressed, the sulfur present in the glass diffused into the solution. Sulfur was traced in the unreacted glass core (Figure 3.30). The sulfur

present in the glass in the form of SO_2 or SO_3 bubbles (formed due to decomposition of $CaSO_4$ during glass preparation) left behind small voids after popping during the reaction.

Some studies were done on the effect of melting duration on the sulfur composition in the glass. Longer durations of melting the reagent grade powders in the furnace resulted in less sulfur content in the glass. The CaLB3-40-S50 glass microspheres used for reaction were melted at 1100°C for 1 hour in the furnace.

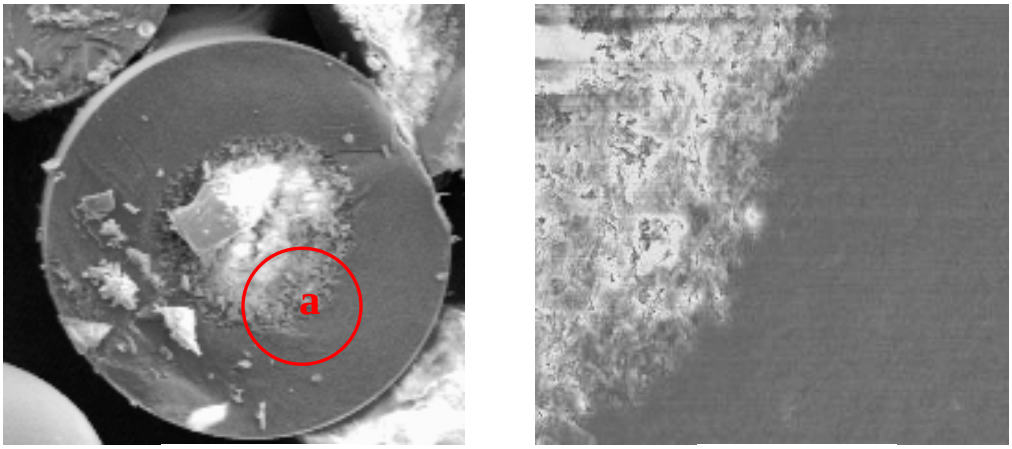

(a) (b)

Figure 3.28: (a) CaLB3-40-S50 microspheres reacted in 0.75 M phosphate solution (pH=10) at 37°C for 8 days. (b) Magnified view of area (a). The region in Figure 41 (b) was mapped by x-rays.

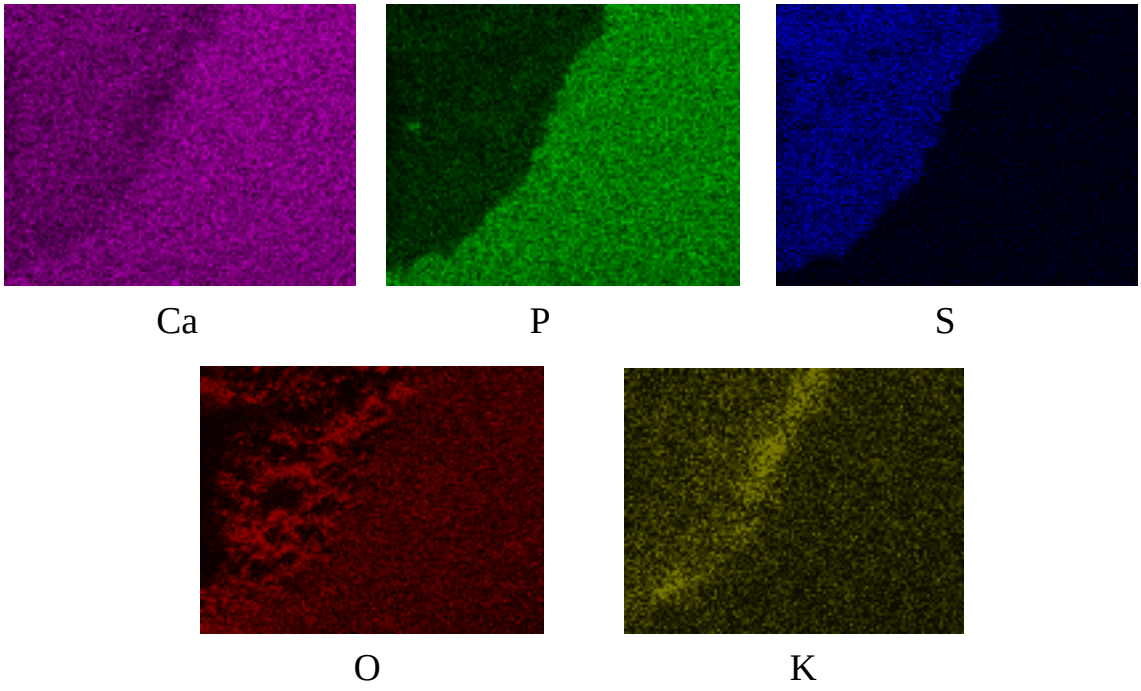

Figure 3.29: X-ray maps for region in Figure 41(b). The unreacted glass core at the center was confirmed by presence of sulfur. The reacted shell comprised of calcium and phosphorus confirming the presence of some form of ACP.

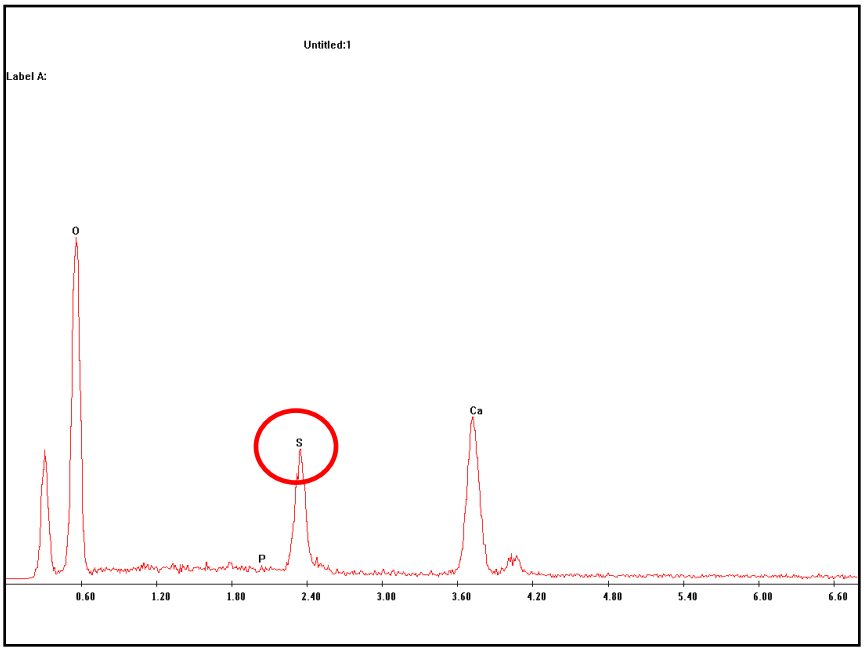

Figure 3.30: EDS spectrum showing presence of sulfur and absence of phosphorus in the glass core.

3.1.5.2.4. <u>XRD characterization</u>. Reacted CaLB3-40-S50 microspheres were characterized by XRD to observe the crystalline phases present. XRD peaks for the as-reacted microspheres contained sharp peaks indicating high crystallinity. The peaks matched the predominant peaks for the stoichiometric HAp and no other crystalline phases were detected in the as-reacted CaLB3-40-S50 microspheres. The XRD patterns for the as-reacted CaLB3-40-S50 microspheres were much more promising than the XRD patterns for as-reacted CaLB3-40-Fears microspheres as the latter one contained broad peaks. In Figure 3.31, both red and blue dots correspond to the crystalline peaks of reacted CaLB3-40-S50 glass microspheres which matched the predominant synthetic HAp peaks.

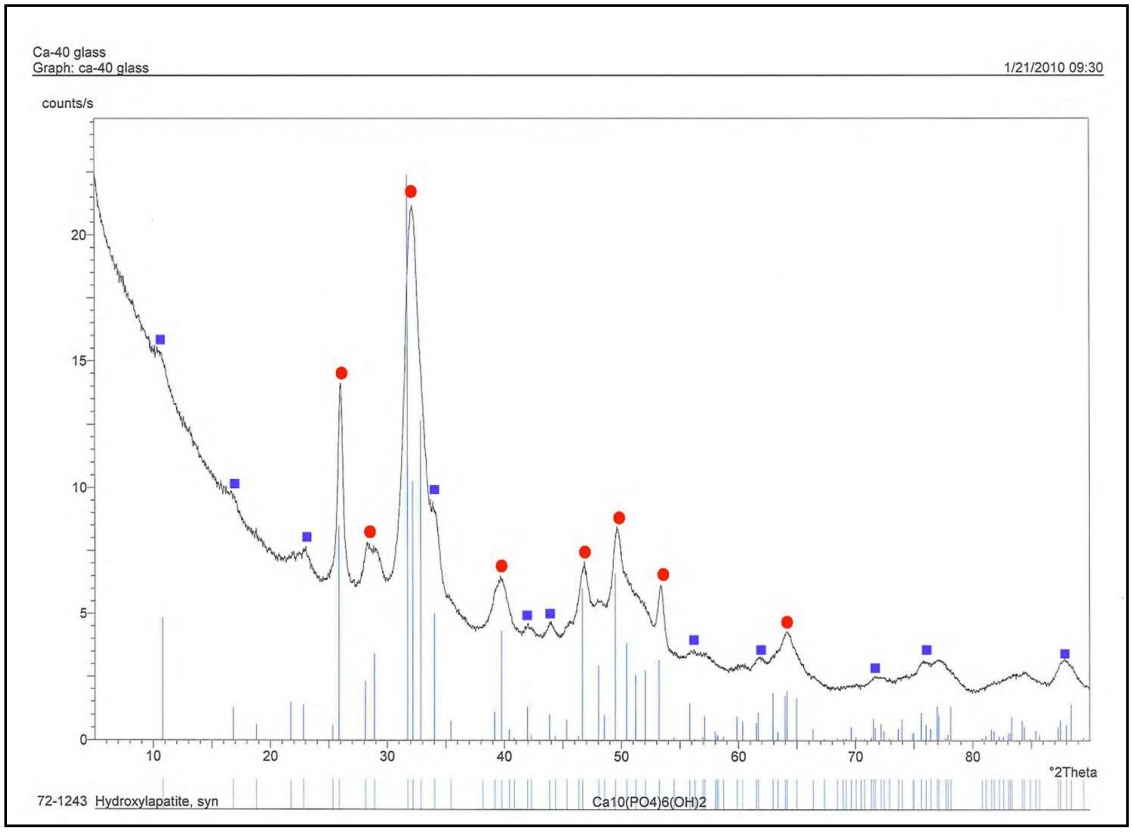

Figure 3.31: XRD pattern showing crystal structure of reacted CaLB3-40-S50 glass microspheres (at 37˚C in 1.0 M phosphate solution for 12 days) with commercial HAp pattern overlaid.

The red dots correspond to the peaks which were earlier matched to confirm the formation of HAp [80]. For reacted CaLB3-40-S50 glass microspheres, even the peaks corresponding to blue dots matched with synthetic HAp peaks which confirmed the formation of more crystalline HAp as compared to HAp formulations in previous research work.

3.1.5.2.5. <u>DTA characterization</u>. DTA analysis of reacted CaLB3-40-S50 glass microspheres revealed the phase transition as they were heat-treated up to 1250˚C in air at a rate of 10˚C/min. Significant dehydration was observed by a broad endothermic peak (Figure 3.32) which signified loss of physically absorbed H_2O. The loss of water was evidenced by the weight loss in the TGA curve. The as-reacted CaLB3-40-S50 glass microspheres lost about 8.5 wt%

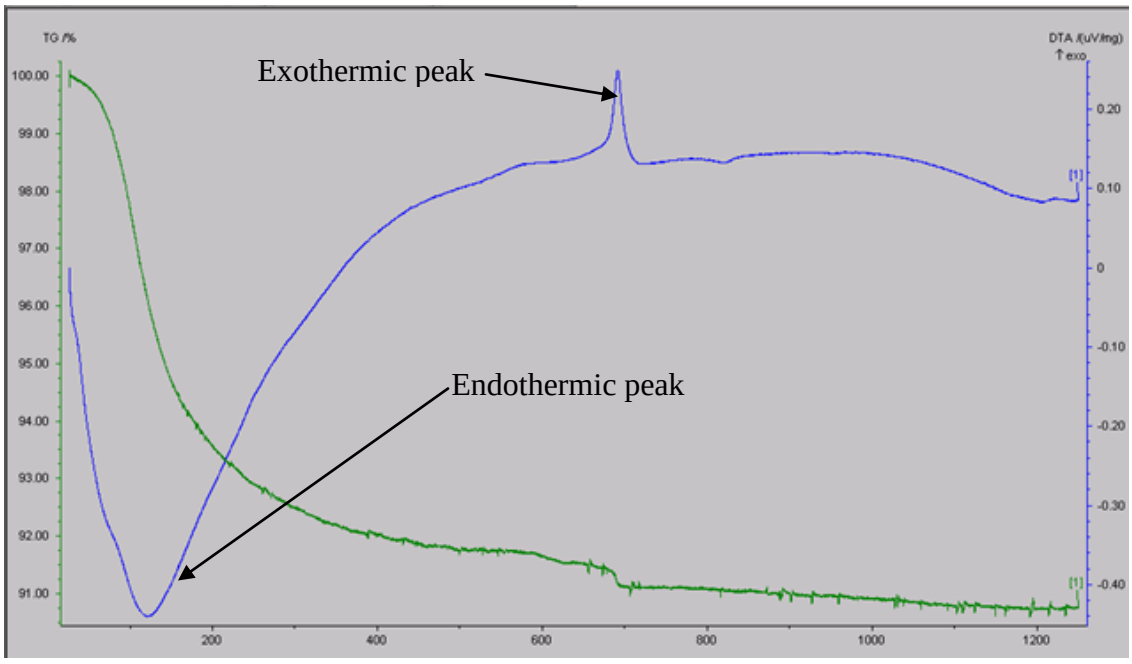

Figure 3.32: DTA and TGA curves measured for as-reacted CaLB3-40-S50 glass microspheres (1.0 M phosphate solution; pH=10; 37˚C; 12 days) heated up to 1250˚C at 10˚C/min.

until a temperature of ~690˚C where the dehydration was completed. An exothermic peak appeared in the DTA curve at around 690˚C, with no corresponding weight change in the TGA curve. This exothermic peak signified that as-reacted CaLB3-40-S50 glass microspheres could have undergone a phase transition as HAp transformed to TCP by loss of H_2O from HAp. Literature supports the phase transition of fully calcium-deficient HAp (Ca/P = 1.5) to TCP when heated above 700˚C (Eq. 2) [77] whereas commercial HAp powders decompose into a mixture of tetra tricalcium phosphate (TTCP) and α-TCP at temperatures above 1360˚C [78]. The low decomposition temperature of as-reacted CaLB3-40-S50 glass microspheres suggest that non-stoichiometric HAp was formed as a result of the precipitation reaction.

$$Ca_9(HPO_4)(PO_4)_5(OH)_{(s)} \longrightarrow 3Ca_3(PO_4)_2 + H_2O_{(g)} \qquad (2)$$

3.1.5.3. CaLB3-40-S75 glass microspheres.

3.1.5.3.1. <u>Effect of concentration of phosphate solution</u>. CaLB3-40-S75 glass microspheres were reacted in K_2HPO_4 solution pH=10 at 37ºC at 0.5 M and 1.0 M concentrations for 6 days and 12 days at each concentration. Table 3.2 lists the d/D values for the reacted microspheres. The readings were taken using Image J software with average value of thickness based on readings for 5 microspheres with five readings for each microsphere.

Table 3.2: Effect of concentration of phosphate solution on d/D ratio of reacted CaLB3-40-S75 microspheres.

Time / Concentration	6 days	12 days
0.50 M	0.64	0.69
1.00 M	1.00	1.00

Table 3.2 shows that CaLB3-40-S75 glass microspheres completely reacted at 1.00 M concentration within 6 days. Figure 3.33 shows cross-sections of reacted CaLB3-40-S75 glass microspheres. The reacted microstructures have more prominent voids as compared to CaLB3-40-S50 microspheres caused by the gas bubbles leaving the particles. The larger sulfur concentration caused more frequent formation of SO_2 bubbles during glass formation.

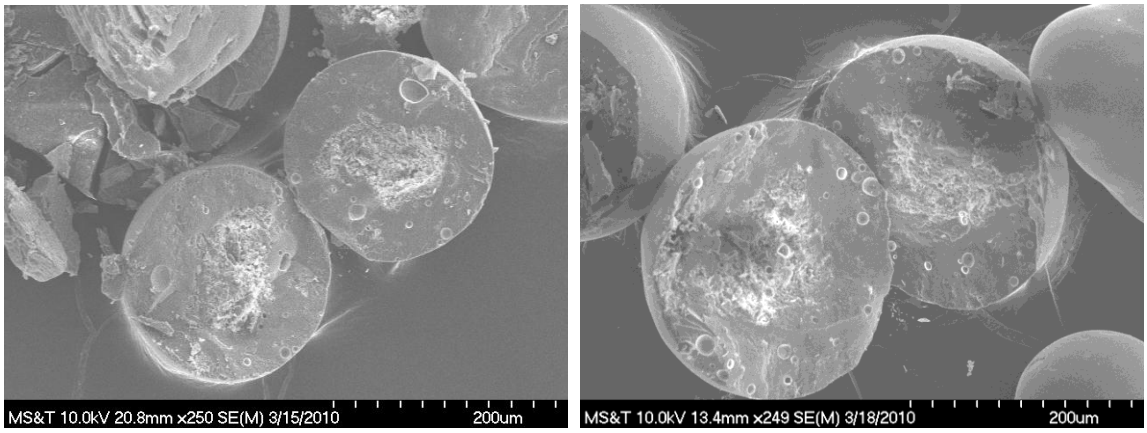

(a) (b)

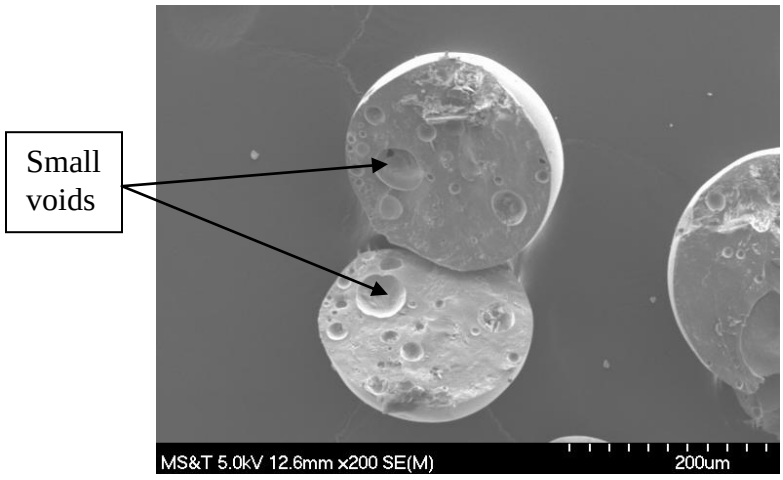

(c)

Figure 3.33: SEM images of CaLB3-40-S75 microspheres reacted at 37°C in (a) 0.5 M phosphate solution (pH=10) for 6 days, (b) 12 days, and (c) 1.0 M phosphate solution (pH=10) for 6 days.

3.1.5.3.2. <u>Effect of pH of phosphate solution</u>. In order to conclude the effect of pH on the microstructure, CaLB3-40-S75 glass microspheres were reacted in 1.0 M K_2HPO_4 solution at pH=8 and 12 (± 0.05) for 6 days at 37°C. No significant difference was observed in the microstructure (Figure 3.34). The reacted microstructures had the same equiaxed grain morphology for different pH values. The quantitative EDS analysis also gave the values of Ca/P ratio ranging from 1.33 to 1.56.

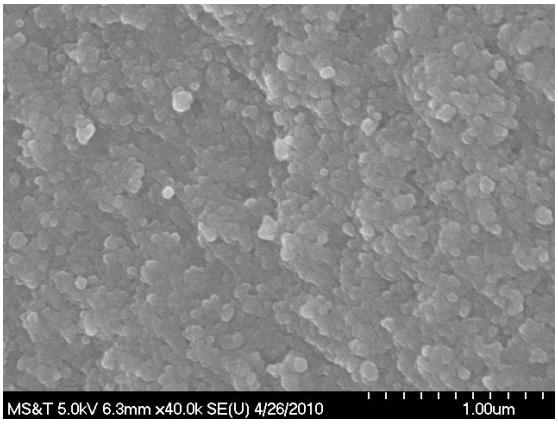

(a)

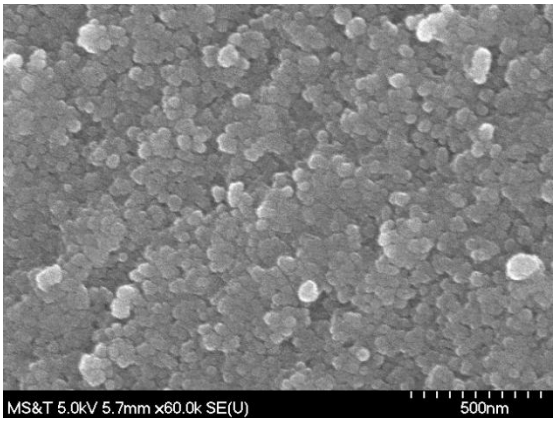

(b)

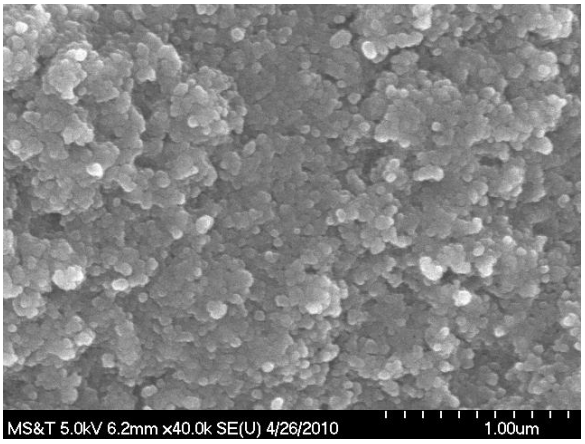

(c)

Figure 3.34: SEM images of CaLB3-40-S75 microspheres reacted at 37°C in 1.0 M phosphate solution for 6 days at (a) pH=8, (b) pH=10, and (c) pH=12.

3.1.5.4. Effect of glass composition, potassium phosphate solution concentration and reaction days on the reacted layer thickness.

3.1.5.4.1. <u>Choice of design of experiments</u>. Various approaches can be used to analyze the effects of numerous factors involved in an experiment. This experiment involved three factors whose effect on the response variable was analyzed by using full factorial design of experiments. The full factorial design is most efficient for this experiment because all the possible treatment combinations of the levels of the factors are investigated in a complete trial. Also, only one factor is changed at a time in a single trial run. The full factorial designs are quite advantageous. They take into account the interactions present amongst the various factors and don't provide any misleading conclusions. Also, factorial designs provide estimation of effects of a factor at varied levels of other factors which are valid over entire range of actual experimental conditions. The change in the response variable, which in this case is the thickness of reacted layer, is attributed to the change in the levels of the three factors, namely:

Factor A = Glass composition (Comp.)

Factor B= Concentration of K_2HPO_4 solution (Conc.)

Factor C = Reaction days (Days)

This is a three-factor factorial experiment with two levels for each factor i.e. 2^3 factorial design.

Levels of A
- A_1 = 50% of CaO coming from $CaSO_4$ and 50% of CaO coming from $CaCO_3$ (denoted with -1 being the lower level)
- A_2 = 75% of CaO coming from $CaSo_4$ and 25% of CaO coming from $CaCO_3$ (denoted with +1 being the higher level)

Levels of B
- B_1 = 0.5 M concentration (denoted with -1 being the lower level)
- B_2 = 1.0 M concentration (denoted with +1 being the higher level)

Levels of C
- C_1 = 6 days (denoted with -1 being the lower level)
- C_2 = 12 days (denoted with +1 being the higher level)

3.1.5.4.2. Experimental procedure. CaLB3-40-S50 and CaLB3-40-S75 glass microspheres were reacted in 0.5 M and 1.0 M K_2HPO_4 solution (pH=10) at 37˚C for 6 days and 12 days. The reaction procedure has been described before in Section 2.2. The response variable i.e. thickness of the reacted HAp layer was measured using Image J software. About 10 measurements were done for each trial run which was further averaged out. Figure 3.35 shows the experimental structure for this experiment.

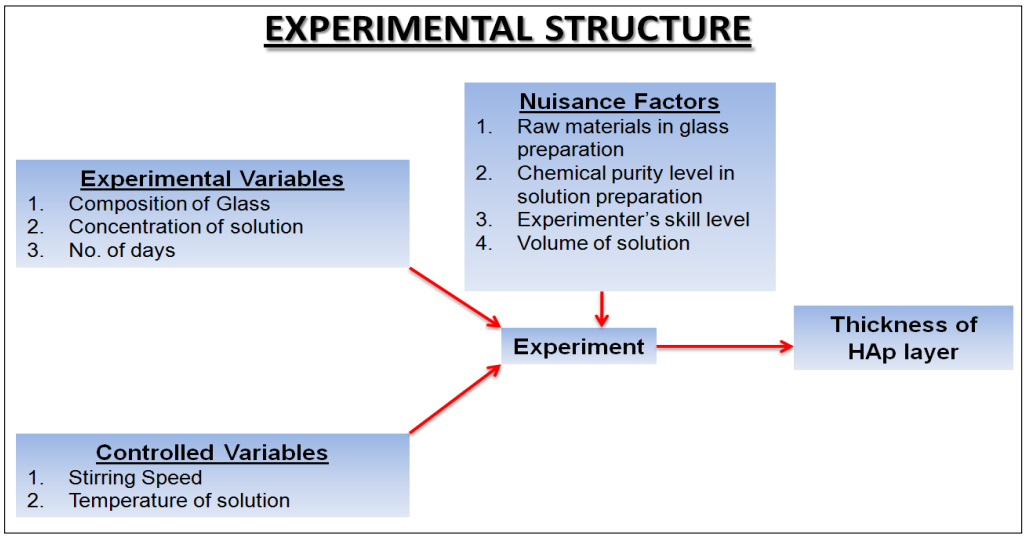

Figure 3.35: Description of experimental variables and response variable.

3.1.5.4.3. <u>Treatment and design structures</u>. Table 3.3 shows all possible treatment combinations in this experiment. The measurand value M_{A1B1C1} was replicated three times by three experimental runs. For the remaining seven treatment combinations, a single replication was carried out due to time constraints. Three values were obtained for the first treatment combination denoted by (1). These three replicated values were then used to generate 14 random numbers based on the standard error obtained from three experimental runs for (1) treatment combination. SAS was used to obtain 14 normally-distributed random numbers from three replications. Hence, 14 replications were generated for remaining seven treatment combinations thereby giving a total of 24 replications for the 8 treatment combinations.

Table 3.3: Treatment combinations for the three factors

	A_1 = 50% - 50%		A_2 = 75% - 25%	
	B_1 = 0.5 M	B_2 = 1.0 M	B_1 = 0.5 M	B_2 = 1.0 M
C_1 = 6 days	(1) M_{A1B1C1}	b M_{A1B2C1}	a M_{A2B1C1}	ab M_{A2B2C1}
C_2 = 12 days	c M_{A1B1C2}	bc M_{A1B2C2}	ac M_{A2B1C2}	abc M_{A2B2C2}

M = Measurand = Thickness of the reacted layer (microns)

(1) = Treatment combination with A, B, and C at lower levels.

a = Treatment combination with A at higher level; B and C at lower levels.

b = Treatment combination with B at higher level; A and C at lower levels.

c = Treatment combination with C at higher level; A and C at lower levels.

ab = Treatment combination with A and B at higher levels; C at lower level.

bc = Treatment combination with B and C at higher levels; A at lower level.

ac = Treatment combination with A and C at higher levels; B at lower level.

abc = Treatment combination with A, B, and C at higher levels.

Table 3.4 lists the values of the response variable.

Table 3.4: Replications of the response variable (microns).

	A_1 = 50% - 50%		A_2 = 75% - 25%	
	B_1 = 0.5 M	B_2 = 1.0 M	B_1 = 0.5 M	B_2 = 1.0 M
C_1 = 6 days	70.44 64.99 68.39	101.41 98.95 99.45	75.46 75.24 75.43	117.92 120.56 122.76
C_2 = 12 days	75.46 66.80 80.81	117.92 119.34 122.36	81.36 82.53 79.75	117.92 124.77 116.69

This experiment was conducted using a completely randomized design. Eight possible treatment combinations were obtained for a 2^3 factorial experiment and after three replications for each treatment combination, 24 observations were obtained in all. After obtaining 24 values for the response variable, the values were randomly picked and input in the SAS for statistical analysis. Table 3.5 lists the randomized design structure for the values of the response variables. The order in which values were input in the SAS software is same as given in Table 3.5.

Table 3.5: Randomized treatment combinations table which was entered in SAS for analysis and effects of the different factors.

Serial No.	Pattern	a	b	c	Reacted Layer
1	ab	1	1	-1	117.92
2	bc	-1	1	1	117.92
3	ab	1	1	-1	120.56
4	(1)	-1	-1	-1	70.44
5	ab	1	1	-1	122.76
6	ac	1	-1	1	81.36
7	abc	1	1	1	117.92
8	a	1	-1	-1	75.46
9	c	-1	-1	1	75.46
10	abc	1	1	1	124.77
11	b	-1	1	-1	101.41
12	(1)	-1	-1	-1	64.99
13	bc	-1	1	1	119.34
14	b	-1	1	-1	98.95
15	a	1	-1	-1	75.43
16	c	-1	-1	1	66.80
17	bc	-1	1	1	122.36
18	ac	1	-1	1	82.53
19	c	-1	-1	1	80.81
20	b	-1	1	-1	99.45
21	ac	1	-1	1	79.75
22	(1)	-1	-1	-1	68.39
23	abc	1	1	1	116.69
24	a	1	1	-1	75.24

3.1.5.4.4. <u>Analysis</u>.

3.1.5.4.4.1. ANOVA. Analysis of Variance (ANOVA) is used to evaluate the significant differences between the means for each factor in an experiment. ANOVA uses estimation of variance to compare the means and can determine if the variation is due to some random error or due to change in the levels of each factor. Sum of squares (SS) of variation are analyzed to account for the variance in the response variable. SS of variation are separated into SS due to variance in the response variable accounted by model and SS due to error. Further, variance ratio (F-value) for main effects and

interactions is obtained by dividing the respective mean square effects with mean square errors (Figure 49). The significance level of the experiment is generally set at 0.05 (α = 0.05). The probability (p-value) of obtaining the F-value being less than 0.05 will lead to the significance of that particular factor or interaction term. The significance of the factors increases if the variance ratio is larger.

3.1.5.4.4.2. Pareto chart. Pareto chart of standardized effects is a graphical representation of the main effects and interactions showing the significance of each factor in the form of horizontal shaded columns. These shaded columns are listed in the order of significance of each effect. The columns exceeding the dotted line are accounted for as significant. In this experiment, there were only two factors involved so linear effects were interpreted. The linear main effects are analyzed as the difference between the average response variable of each factor at high and low levels. Also, two-way linear interaction effects are analyzed as half the difference between the high/low level of one factor and high/low level of another factor.

3.1.5.4.5. Results. From the ANOVA table above (Figure 3.36), it was concluded that the p-value of three factor interaction term (0.0023) was less than 0.05. Hence, it is significant. Further, the two way interaction terms were analyzed and interaction of composition of glass and number of days of reaction is quite significant as its p-value (0.0015) is less than the significance level. Finally the main effects were looked at and it was clearly evident that the p-values for each of the main factors were less than 0.05. Hence, the main factors are quite significant.

The GLM Procedure

Dependent Variable: reaction

Source	DF	Sum of Squares	Mean Square	F Value	Pr > F
Model	7	10910.96443	1558.70920	136.76	<.0001
Error	16	182.36287	11.39768		
Corrected Total	23	11093.32730			

R-Square	Coeff Var	Root MSE	reaction Mean
0.983561	3.558867	3.376045	94.86292

Source	DF	Type I SS	Mean Square	F Value	Pr > F
a	1	451.273537	451.273537	39.59	<.0001
b	1	9736.078838	9736.078838	854.22	<.0001
a*b	1	13.969004	13.969004	1.23	0.2846
c	1	373.749337	373.749337	32.79	<.0001
a*c	1	167.534504	167.534504	14.70	0.0015
b*c	1	18.709004	18.709004	1.64	0.2184
a*b*c	1	149.650204	149.650204	13.13	0.0023

Source	DF	Type III SS	Mean Square	F Value	Pr > F
a	1	451.273537	451.273537	39.59	<.0001
b	1	9736.078838	9736.078838	854.22	<.0001
a*b	1	13.969004	13.969004	1.23	0.2846
c	1	373.749337	373.749337	32.79	<.0001
a*c	1	167.534504	167.534504	14.70	0.0015
b*c	1	18.709004	18.709004	1.64	0.2184
a*b*c	1	149.650204	149.650204	13.13	0.0023

Figure 3.36: ANOVA table showing significance of the main effects and interaction terms.

The standardized effects chart (Figure 3.37) shows that concentration of the solution has the most significant effect on the thickness of reacted layer (conversion rate) amongst all the factors, followed by composition of glass; number of days of reaction; two-way interaction of composition of glass and duration of reaction; and three way interaction between the factors.

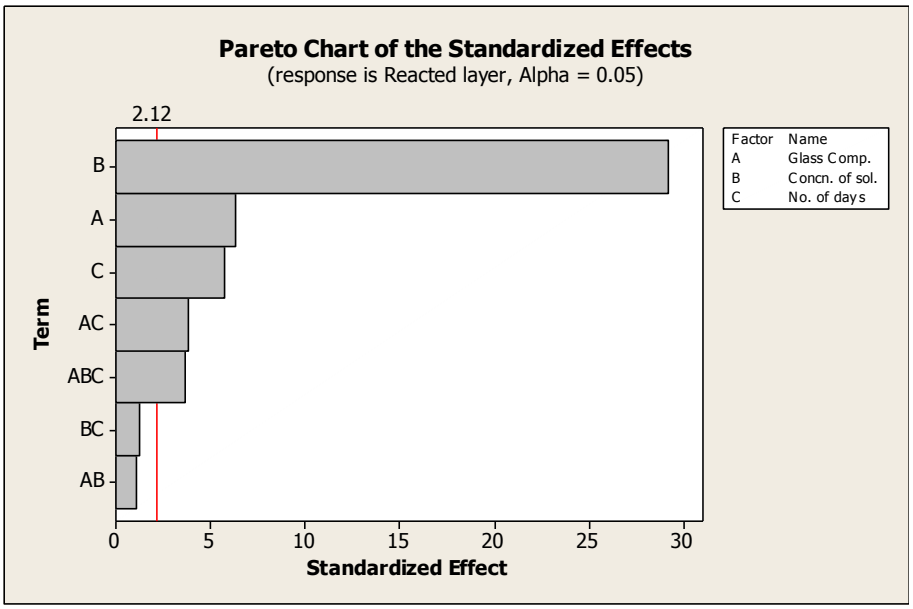

Figure 3.37: Standardized effects showing the significance of the

Figure 3.38 shows the variation of the main effects and their corresponding significance. High variation is seen for the concentration effect which supports the highest significance of concentration of solution on the conversion rate (thickness of reacted layer). Composition of glass and number of days of reaction do not show much variation between high and low levels but they are still significant.

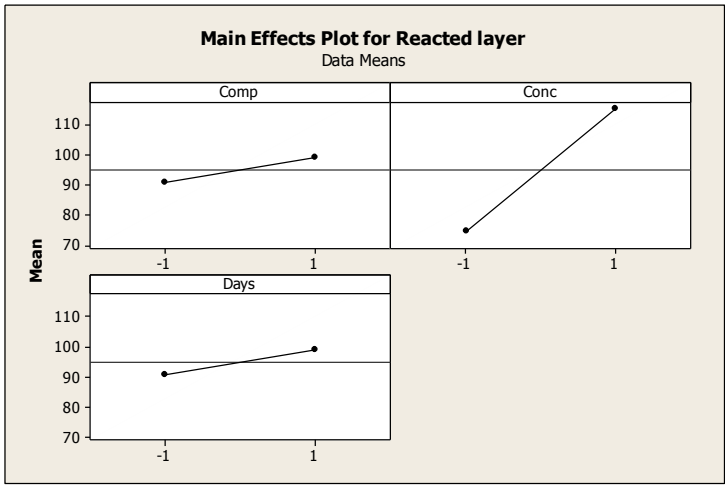

Figure 3.38: Plot of main effects for the reacted layer.

Figure 3.39 shows the two-way interaction of the three factors. Composition of glass * number of days interaction shows more variation comparatively to the other two graphs which proves its significance on the conversion rate (reacted layer thickness). The lines corresponding to the interaction of concentration of solution* number of days of reaction and composition of glass* concentration of solution are approximately parallel, indicating lack of interaction.

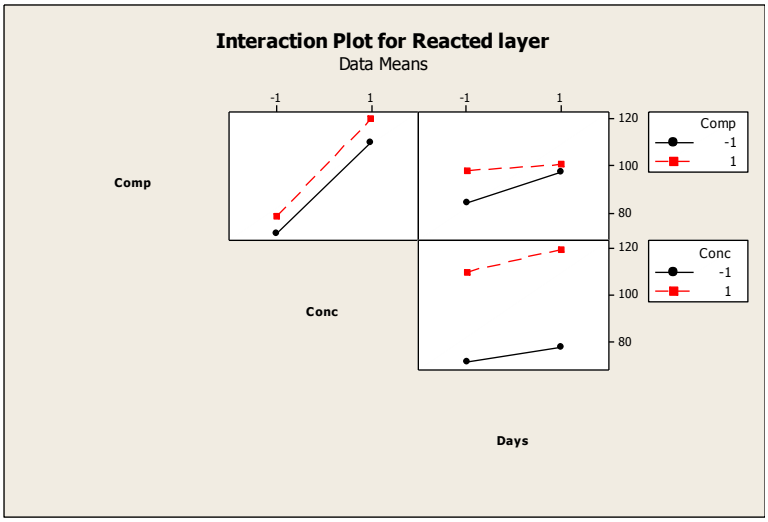

Figure 3.39: Plot of interactions for the reacted layer.

3.1.6. Heat-Treatment of As-Reacted CaLB3-40-S50 Microspheres.

3.1.6.1. Effect on the microstructure. The as-reacted CaLB3-40-S50 microspheres were heat-treated at 300°C, 600°C, 900°C, and 1200°C for 1 hour at each temperature value. The heat-treatment temperature had a considerable effect on the microstructure of HAp grains and the porosity of the microspheres. Figure 3.40 shows the internal microstructure of the as-reacted microspheres. Heat-treatment at 300°C did not cause any significant change in the morphology of the grains (Figure 3.41).

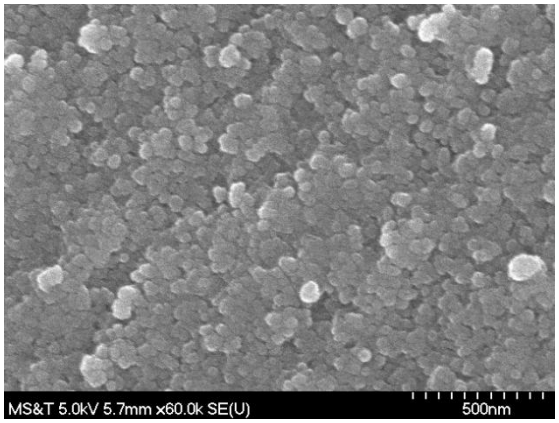

Figure 3.40: Internal microstructure of as-reacted CaLB3-40-S50 microspheres. Equiaxed grains can be seen in the microstructure.

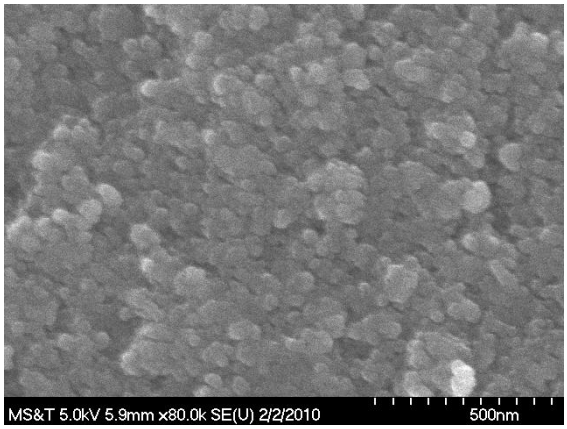

Figure 3.41: Internal microstructure of as-reacted CaLB3-40-S50 microspheres heat treated at 300°C for 1 hour. No significant change could be seen in the microstructure.

Heat treatment at 600°C for 1 hour caused coarsening of grains with increase in the pore size and initiated the process of grain growth (Figure 3.42).

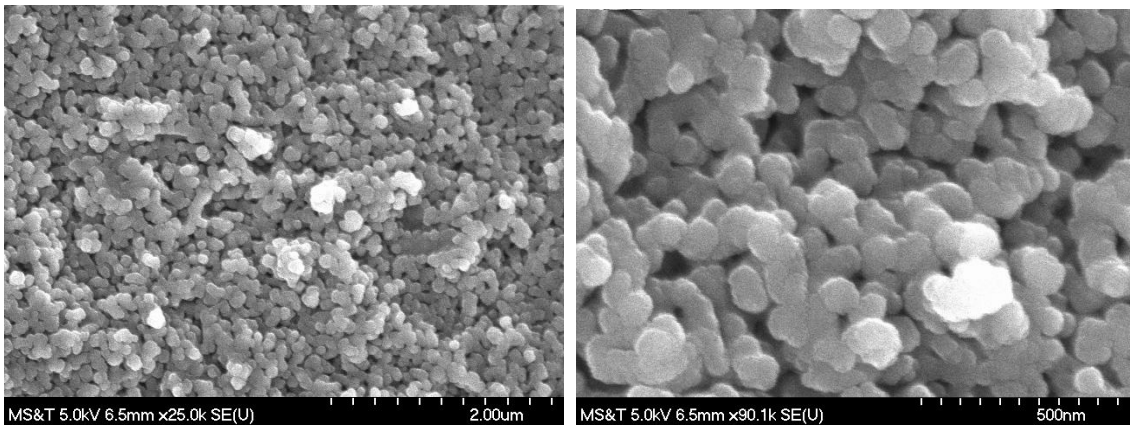

Figure 3.42: Internal microstructure of as-reacted CaLB3-40-S50 microspheres heat treated at 600°C for 1 hour resulting in normal grain growth.

Further heat treatment at 900°C for 1 hour caused the grains to start coalescing with decrease in the specific area (Figure 3.43). The coalescence temperature for Ca-deficient HAp is generally below 1000°C [65].

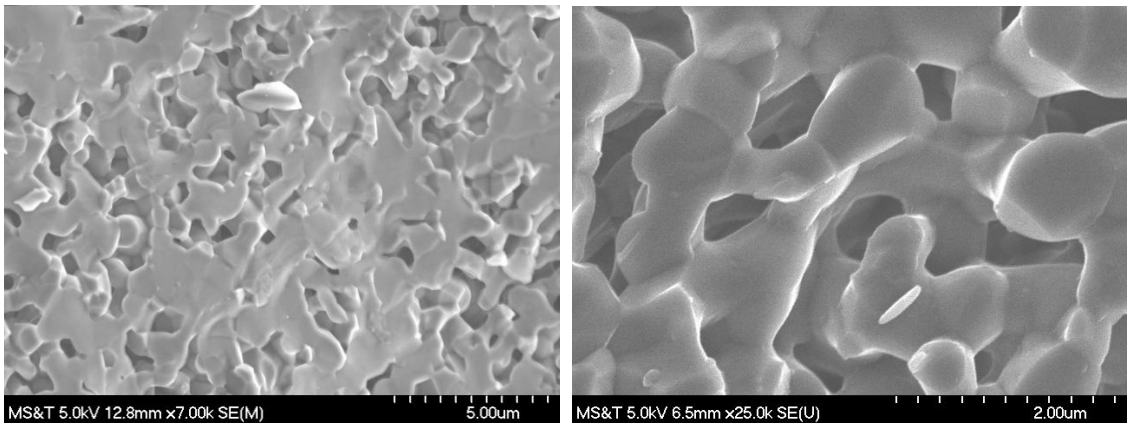

Figure 3.43: Internal microstructure of as-reacted CaLB3-40-S50 microspheres heat treated at 900°C for 1 hour.

Further sintering at 1200°C for 1 hour completely closed all open porosity resulting in formation of an impermeable solid microsphere (Figure 3.44).

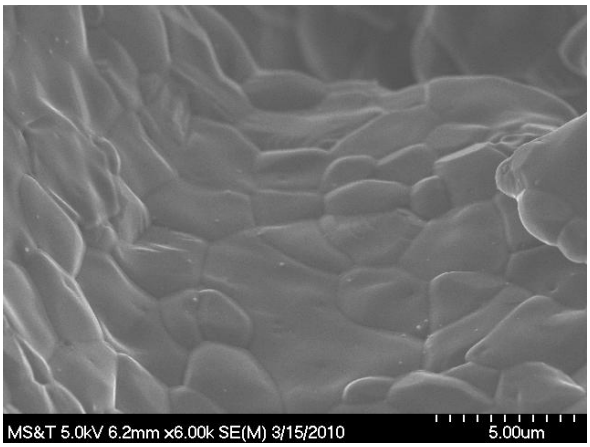

Figure 3.44: Internal microstructure of as-reacted CaLB3-40-S50 microspheres heat treated at 1200°C for 1 hour.

3.1.6.2. Effect on the volume of as-reacted microspheres. The as-reacted CaLB3-40-S50 glass microspheres shrunk in the volume as they were heat-treated at 600˚C and 900˚C. No significant reduction was observed in the diameter as the reacted microspheres were heat-treated at 300˚C. The diameter of the microspheres was measured on a Keyence® optical microscope (Figure 3.45). The average diameter of the as-reacted microspheres was about 265 µm. The average diameter of the microspheres reduced to about 215 µm when heat-treated at 600˚C and further reduced to 185 µm at 900˚C. The size distribution for various batches of microspheres is shown in Figure 3.46. The average volume percent shrinkage (as compared to initial volume of as-reacted microspheres) was about 80% (at 600˚C) and increased to about 86% (at 900˚C). Heat-treatment at 1200˚C did not cause much shrinkage in the volume. Figure 3.47 shows the decrease in the average volume percentage when the as-reacted CaLB3-40-S50 microspheres were heat-treated at 600˚C, 900˚C, and 1200˚C. Each data point in this graph has been averaged for at least 50 microspheres.

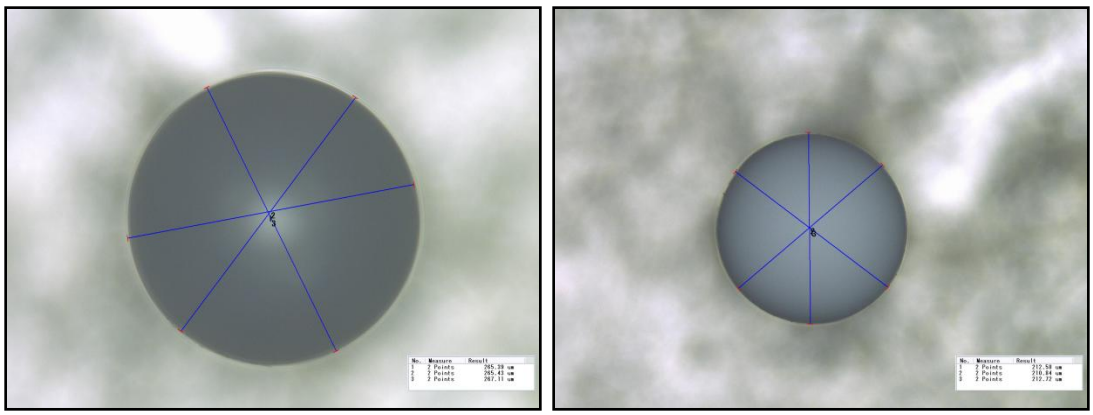

Figure 3.45: Diameter of the microspheres from each batch measured under Keyence® optical microscope

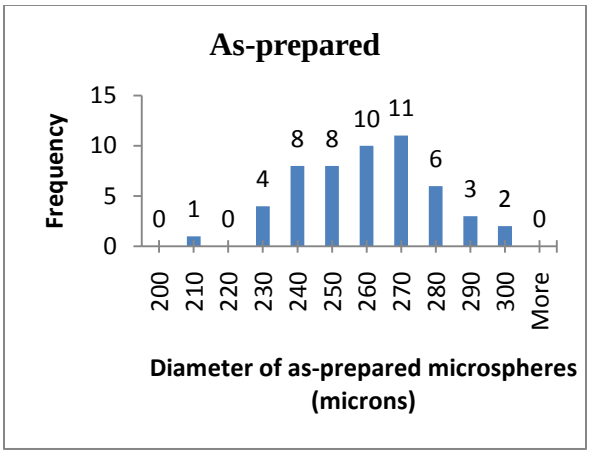

(a)

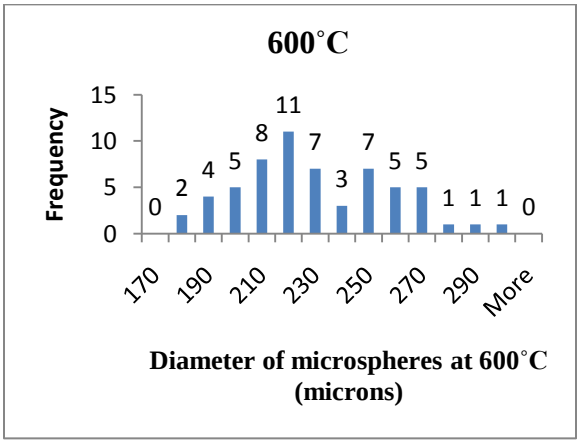

(b)

Figure 3.46: Size distribution of as-prepared CaLB3-40-S50 microspheres heat-treated at various temperatures.

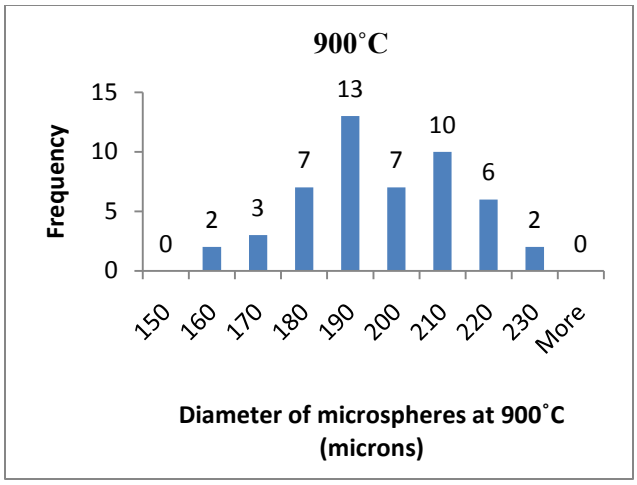

(c)

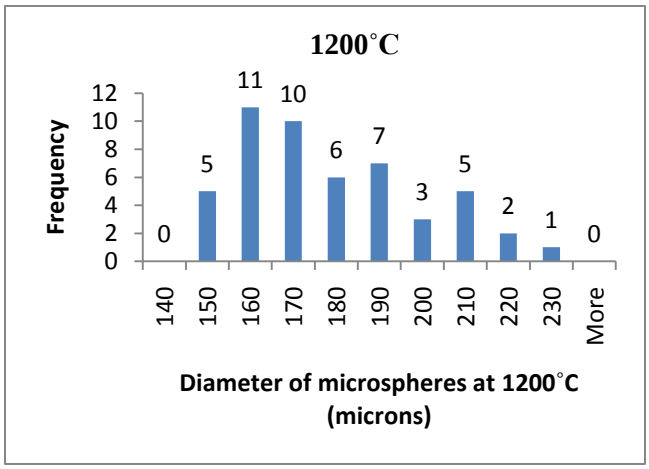

(d)

Figure 3.46: Size distribution of as-prepared CaLB3-40-S50 microspheres heat-treated at various temperatures (Contd.).

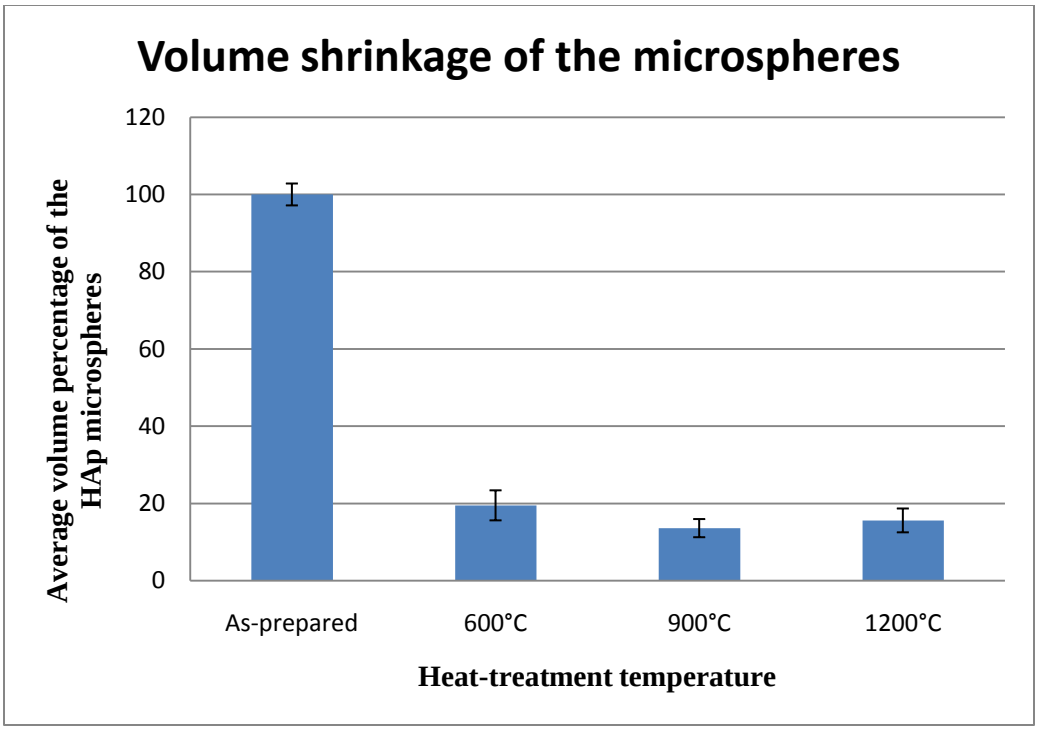

Figure 3.47: Volume percentage shrinkage of HAp microspheres with heat-treatment temperature.

3.1.7. Compressive Strength. The as-reacted CaLB3-40-S50 microspheres and as-reacted CaLB3-40-S50 microspheres heat-treated at 600˚C, 900˚C, and 1200˚C were ruptured on an Instron press using a ± 50 N static load cell to calculate the crushing force. The crushing force did not increase as the microspheres were heat-treated at 600˚C and 900˚C. There was significant increase in the crushing force for the as-reacted microspheres heat-treated at 1200˚C due to enhanced densification and coalescence of the grains (Figure 3.48). Also, the crushing force increased with increase in diameter of the microspheres for a given batch of microspheres. About 25-30 microspheres were measured from each batch for calculating the crushing force. Figure 3.49 shows the ruptured microspheres after the compression testing. For a single batch of microspheres

(e.g. as-reacted microspheres), the values of crushing force varied for two quite similar values of diameter. The reason for this scattered data is influence of remaining microporosity, inherent defects, variations in grain size, impurities, etc. It has been reported before that grain size and porosity have an influence on the fracture path [29].

The reason for calculating the crushing force and not calculating the mechanical strength is because of non-uniform cross sections of the microspheres. The exact contact area at which fracture occurs cannot be determined. Due to variation in the cross-sections across the microspheres, there will be tri-axial stress distribution. Hence, the value of compressive load acting at the point when contact occurs between the force rod and microsphere would not be equal to the compressive load acting at the instant of rupture.

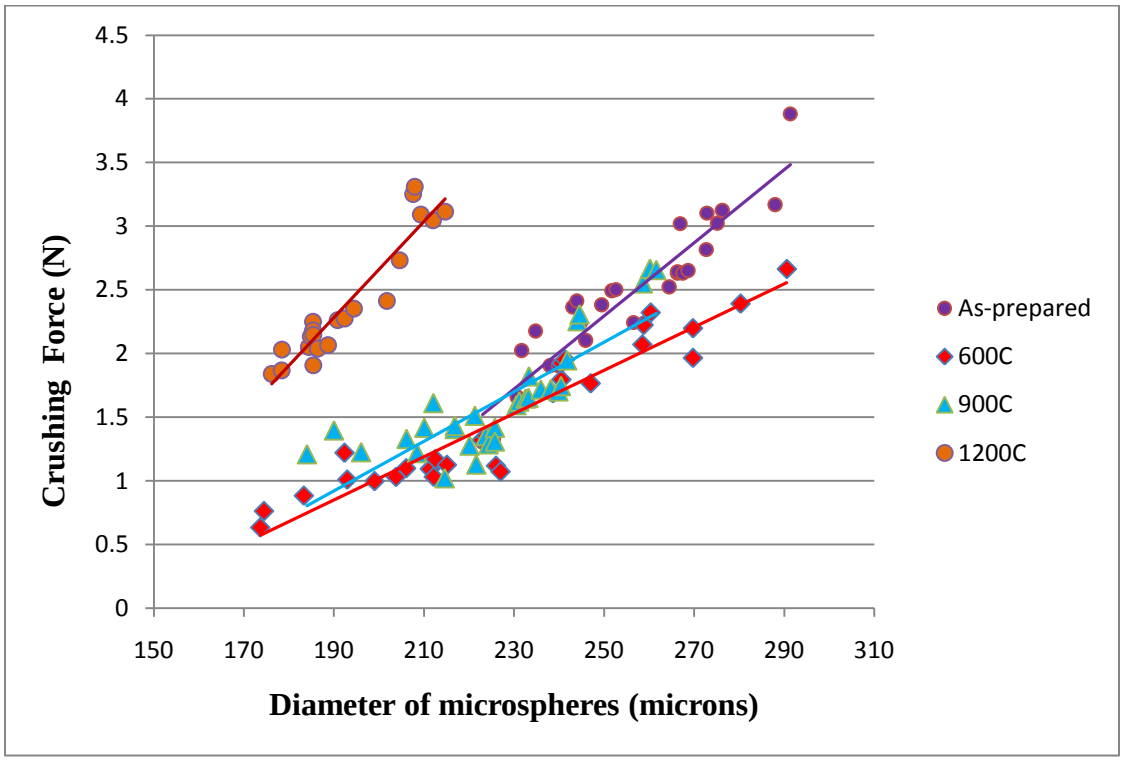

Figure 3.48: Crushing force of as-reacted and as-reacted CaLB3-40-S50 microspheres heat treated at 600˚C, 900˚C, and 1200˚C.

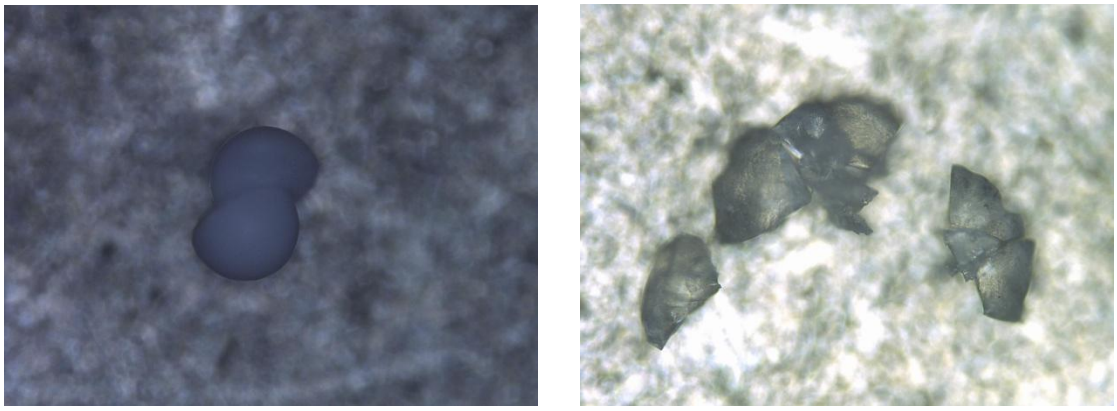

Figure 3.49: Ruptured as-reacted CaLB3-40-S50 microspheres after the test.

However, the mechanical strength of the as-reacted CaLB3-40-S50 microspheres was calculated in accordance with previous approach [76]. The average diameter of the as-reacted microspheres was about 265 μm. The extension of the force rod was calculated which gave the value of contact area corresponding to the point of rupture. The mechanical strength of as-reacted microspheres was 85 ± 5 MPa which was quite high as compared to mechanical strength of hollow CaLB3 microspheres [76]. Utmost care was taken in testing a complete spherical microsphere as deviation from perfect spherical geometry could affect the mechanical strength. However, the possibility of such deviation cannot be ruled out.

4. CONCLUSIONS

The following conclusions could be made from the results of this research:

1. Successful conversion of CaLB3-40-S50 and CaLB3-40-S75 bioactive glass microspheres to solid but porous HAp microspheres.

2. Fears's conclusions validated for conversion of CaLB3-MoSci bioactive glass microspheres according to which CaLB3 glasses containing CaO < 40 wt% yield hollow microstructures whereas CaLB3 glasses containing CaO ≥ 40 wt% yield solid but porous microstructures.

3. Presence of sulfur has an effect on the conversion rate of the bioactive glass microspheres.

4. EDS and DTA analysis evidenced the formation of calcium-deficient HAp.

5. XRD patterns revealed formation of a comparatively better crystalline form of HAp.

6. No change in the microstructure of HAp due to change in the pH of the phosphate solution.

7. Statistical analysis performed for the effect of composition of glass, concentration of potassium phosphate solution, and number of days of reaction on the reaction rate yielded the following conclusions:

- The concentration of the potassium phosphate solution has the most significant effect on the reacted layer thickness (conversion rate) followed by composition of the bioactive glass and number of days of reaction. This implies that 1.0 M phosphate solution will produce much thicker reacted layer and consequently the reaction rate will increase.

- The two-way interaction of composition of glass and number of days of reaction has also significant effect on the reaction which implies that CaLB3-40-S75 glass microspheres require less number of days of reaction to get completely converted.
- The three-way interaction of composition of glass, concentration of solution and reaction days is also significant. Hence, the combination which gives best reaction outcome is CaLB3-40-S75 glass microspheres reacted in 1.0 M potassium phosphate solution for 6 days.

8. Heat-treatment at 600˚C, 900˚C, and 1200˚C caused a change in the microstructure closing off all open porosity at 1200˚C.

9. Volume shrinkage occurred as the HAp microspheres were heat-treated to 600˚C and 900˚C.

10. Solid but porous HAp microspheres were mechanically stronger (85 ± 5 MPa) as compared to hollow HAp microspheres.

11. Crushing force of HAp microspheres increased with increase in the diameter of the microspheres. The increase was faster at the highest temperature of heat-treatment of 1200˚C.

BIBLIOGRAPHY

[1] L. L. Hench and J. Wilson, An Introduction to Bioceramics, World Scientific, New Jersey (1993).

[2] K. A. Hing, S. M. Best, and W. Bonfield, "Characterization of porous hydroxyapatite," Journal of Materials Science: Materials in Medicine, 10 (1999) 135.

[3] J. C. Merry, I. R. Gibson, S. M. Best, and W. Bonfield, "Synthesis and characterization of carbonate hydroxyapatite," Journal of Materials Science: Materials in Medicine, 9 (1978) 779.

[4] W. C. O'Neill, "The fallacy of the calcium–phosphorus product," Kidney International, 72 (2007) 792.

[5] R. V. da Silva, C. A. Bertran, E. Y. Kawachi, and J. A. Camilli, "Repair of cranial bone defects with calcium phosphate ceramic implant or autogenous bone graft," Journal of Craniofacial Surgery, 18 (2007) 281.

[6] T. J. Webster, R. W. Siegel, and Bizios, "Enhanced functions of osteoblasts on nano phase materials," Biomaterials, 21 (2000) 1803.

[7] A. El-Ghannan, P. Ducheyne, and I. M. Shapiro, "Effect of serum proteins on osteoblast adhesion to surface-modified bioactive glass and hydroxyapatite," Journal of Orthopaedic Research, 17 (1999) 340.

[8] Y. Harada, J. T. Huang, V. A. Doppalapudi, A. A. Willis, M. Jasty, and W. H. Harris, "Differential effects of different forms of hydroxyapatite and hydroxyapatite/tricalcium phosphate particulates on human monocyte/macrophages in vitro," Journal of Biomedical Materials Research, 31 (1996) 19.

[9] J. S. Sun, Y. H. Tsuang, W. H. S. Chang, J. Li, H. C. Liu, and F. H. Lin, "Effect of hydroxyapatite particle size on myoblasts and fibroblasts," Biomaterials, 18 (1997) 683.

[10] B. Viswanath and N. Ravishankar, "Controlled synthesis of plate-shaped hydroxyapatite and implications for the morphology of the apatite phase in bone," Biomaterials, 29 (2008) 4855.

[11] S. Weiner and H. D. Wagner, "The material bone: structure–mechanical function relations," Annual Review of Materials Science, 28 (1998) 271.

[12] C. P. A. T. Klein, A. A. Driessen, and K. De Groot, “Relationship between the degradation behaviour of calcium phosphate ceramics and their physical/chemical characteristics and ultrastructural geometry,” Biomaterials, 5 (1984) 157.

[13] S. L. Gunderson and R. C. Schiavone, in International Encyclopedia of Composites, edited by S. M. Lee (VCH Publishers, Inc., New York, 1991), vol. 5, p. 324.

[14] J. D. Currey, in Handbook of Composites, edited by A. Kelly and S. T. Mileiko (Elsevier Science Publishers B. V., 1983), vol. 4, p. 501.

[15] J. L. Katz, in Symposia of the Society for Experimental Biology, Number XXXIV: The mechanical properties of biological materials (Cambridge University Press, 1980), p. 99.

[16] M. Iijima, H. Kamemizu, N. Wakamatsu, T. Goto, Y. Doi, and Y. Moriwaki, “Transition of octacalcium phosphate to hydroxyapatite in solution at pH 7.4 and 37 C,” Journal of Crystal Growth, 181 (1997) 70.

[17] Y. Liu, W. Wu, G. Sethuraman, and G. H. Nancollas, “Intergrowth of calcium phosphates: an interfacial energy approach,” Journal of Crystal Growth, 174 (1997) 386.

[18] P. G. Koutsoukos and G. H. Nancollas, “The morphology of hydroxyapatite crystals grown in aqueous solution at 37 C,” Journal of Crystal Growth, 55 (1981) 369.

[19] X. Lu and Y. Leng, “Theoretical analysis of calcium phosphate precipitation in simulated body fluid,” Biomaterials, 26 (2005) 1097.

[20] C. P. A. T. Klein, J. M. A. de Blieck Hogerworst, J. G. C. Wolke, and K. de Groot, “Studies of solubility of different calcium phosphate ceramic particles in vitro,” Biomaterials, 11 (1990) 509.

[21] F. J. G. Cuisinier, P. Steuer, A. Brisson, and J. C. Voegel, “High resolution electron microscopy study of crystal growth mechanisms in chicken bone composites,” Journal of Crystal Growth, 156 (1995) 443.

[22] M. D. Grynpas and S. Omelon, “Transient precursor strategy of very small biological apatite crystals,” Bone, 41 (2007) 162.

[23] C. Benaqqa and J. Chevalier, “Slow crack growth behavior of hydroxyapatite ceramics,” Biomaterials, 26 (2005) 6106.

[24] K. E. Tanner, R. N. Downes, and W. Bonfield, "Clinical applications of hydroxyapatite reinforced materials," British Ceramic Transactions, 93 (1994) 104.

[25] W. Suchanek and M. Yoshimura, "Processing and properties of hydroxyapatite-based biomaterials for use as hard tissue replacement implants," Journal of Materials Research, 13 (1998) 94.

[26] A. Royer, J. C. Viguie, M. Heughebaert, and J. C. Heughebaert, "Stoichiometry of hydroxyapatite: influence on the flexural strength," Journal of Materials Science: Materials in Medicine, 4 (1993) 76.

[27] H. Monma, T. Kamiya, M. Tsutsumi, and Y. T. Hasegawa, "Comparative study on compaction and sintering properties of hydroxyapatite powders," Gypsum & Lime, 208 (1987) 127.

[28] R. Z. LeGeros, "Calcium phosphates in oral biology and medicine," in Monographs in Oral Sciences, vol. 15, ed. H. Myers and S. Karger, Basel, 1991.

[29] K. Yamashita and T. Kanazawa, Inorganic Phosphate Materials, edited by T. Kanazawa (Materials Science Monograph 52, Kodansha & Elsevier, 1989) p. 15.

[30] L. L. Hench, "Bioceramics: from concept to clinic," Journal of American Ceramic Society, 74 (1991) 1487.

[31] E. C. Shors and R. E. Holmes, An Introduction to Bioceramics, edited by L. L. Hench and J. Wilson, Adv. Ser. Ceram. 1 (World Scientific Publishing Co. Pte. Ltd., London, Hong Kong, Singapore, 1993) p. 181.

[32] D. M. Liu, "Porous hydroxyapatite bioceramics," Key Engineering Materials, 115 (1996) 209.

[33] D. M. Liu, "Control of pore geometry on influencing the mechanical property of porous hydroxyapatite bioceramic," Journal of Materials Science Letters, 15 (1996) 419.

[34] Li-Hong He, Owen C. Standard, Tiffany T.Y. Huang, Bruno A. Latella, and Michael V. Swain, "Mechanical behaviour of porous hydroxyapatite," Acta Biomaterialia, 4 (2008) 577.

[35] M. Jarcho, "Biomaterial aspects of calcium phosphates," Dental Clinics of North America, 30 (1986) 25.

[36] R. Holmes, V. Mooney, R. Bucholz, and A. Tencer, "A coralline hydroxyapatite bone graft substitute clinical orthopaedics and related research," Clinical Orthopaedics and Related Research, 188 (1984) 252.

[37] S. M. Barinov and V. Y. Shevchenko, "Dynamic fatigue of porous hydroxyapatite bioceramics in air," Journal of Material Science Letters, 14 (1995) 582.

[38] G. Daculsi, F. Jegoux, and P. Layrolle, "The micro macroporous biphasic calcium phosphate concept for bone reconstruction and tissue engineering," in Advanced Biomaterials: Fundamentals, Processing and Applications, edited by B. Basu, D. S. Katti, and A. Kumar, Wiley-American Ceramic Society, (2009) p. 768.

[39] J. M. Cordell, M. L. Vogle, and A. J. Wagoner Johnson, "The influence of micropore size on the mechanical properties of bulk hydroxyapatite and hydroxyapatite scaffolds," Journal of Mechanical Behavior of Biomedical Materials, 2 (2009) 560.

[40] R. Hodgkinson and J. D. Currey, "The effect of variation in structure on the Young's modulus of cancellous bone: a comparison of human and non-human material," Journal of Engineering in Medicine," 204 (1990) 115.

[41] O. Prokopiev and I. Sevostianov, "Dependence of the mechanical properties of sintered hydroxyapatite on the sintering temperature," Materials Science Engineering A, 431 (2006) 218.

[42] M. Vogel, C. Voigt, U. M. Gross, and C. M. Müller-Mai, "In vivo comparison of bioactive glass particles in rabbits," Biomaterials, 22 (2001) 357.

[43] L. L. Hench and J. Wilson, "Surface-active biomaterials," Science, 226 (1984) 630.

[44] J. A. Wojick, "Hydroxyapatite formation on a silicate and borate glass," M.S. Thesis, University of Missouri-Rolla (1999).

[45] A. Osaka, S. Hayakawa, K. Tsuru, and C. Ohtsuki, "Bioactivity of alkali and alkaline earth borosilicate glasses," in Borate Glasses, Crystals & Melts, A. C. Wright, S. A. Feller and S. C. Hannon (eds.), Society of Glass Technology, Sheffield, U.K., (1984) 490.

[46] H. Aoki, "Science and medical applications of hydroxyapatite," (JAAS, Tokyo, 1991).

[47] E. B. Jaffee, Geological Survey Circular, 135 (1951).

[48] H. S. Liu, T. S. Chin, L. S. Lai, S. Y. Chiu, K. H. Chung, C. S. Chang, and M .T. Lui, "Hydroxyapatite synthesized by a simplified hydrothermal method," Ceramics International, 23 (1997) 19.

[49] J. Li, H. Liao, and M. Sjöström, "Characterization of calcium phosphates precipitated from simulated body fluid of different buffering capacities," Biomaterials, 18 (1997) 743.

[50] C. Liu, Y. Huang, W. Shen, and J. Cui, "Kinetics of hydroxyapatite precipitation at pH 10 to 11," Biomaterials, 22 (2001) 301.

[51] K. P. Fears, "Formation of hollow hydroxyapatite microspheres," M.S. Thesis, University of Missouri-Rolla (2001).

[52] D. E. Day, J. E. White, R. F. Brown, and K. D. McMenamin, "Transformation of borate glasses into biologically useful materials," Glass Technology, 44 (2003) 75.

[53] S. D. Conzone, "Non-uniform reaction of dysprosium lithium borate glasses with aqueous solutions," Ph.D. Thesis, University of Missouri-Rolla (1999).

[54] A. Paul, "Chemical durability of glasses: a thermodynamic approach," Journal of Materials Science, 12 (1977) 2246.

[55] S. S. Zumdahl, "Chemical Principles," DC Health and Co. Lexington, KY (1995).

[56] S. D. Conzone, "Biodegradable dysprosium lithium borate glasses for radiation Synovectomy," M. S. Thesis, University of Missouri-Rolla (1996).

[57] B. C. Bunker, "Molecular mechanisms for corrosion of silica and silicate glasses," Journal of Non-Crystalline Solids, 179 (1994) 300.

[58] H. Dislich and E. Hussmann, "Amorphous and crystalline dip coatings obtained from organometallic solutions: procedures, chemical processes, and products," Thin Solid Films, 77 (1981) 129.

[59] A. W. Adamson, Physical Chemistry of Surfaces, 5^{th} edition, John Wiley and Sons, Inc., New York, (1990).

[60] S. Stea, M. Visentin, L. Savarino, M. E. Donati, A. Pizzoferruto, A. Moroni, and V. Caia, "Quantitative analysis of the bone-hydroxyapatite coating interface," Journal of Materials Science: Materials in Medicine, 6 (1995) 455.

[61] K. A. Khalil, S. W. Kim, N. Dharmaraj, K. W. Kim, and H. Y. Kim, "Novel mechanism to improve toughness of the hydroxyapatite bioceramics using high frequency induction heat sintering," Journal of Materials Processing Technology, 187–188 (2007) 417.

[62] A. J. Ruys, M. Wei, C. C. Sorrell, M. R. Dickson, A. Brandwood, and B. K. Milthorpe, "Sintering effect on the strength of hydroxyapatite," Biomaterials, 16 (1995) 409.

[63] P. Van Landuyt, F. Li, J. P. Keustermans, J. M. Streydio, F. Delannay, and E. Munting, "The influence of high sintering temperatures on the mechanical properties of hydroxylapatite," Journal of Materials Science: Materials in Medicine, 6 (1995) 8.

[64] N. Y. Mostafa, "Characterization, thermal stability and sintering of hydroxyapatite powders prepared by different routes," Materials Chemistry and Physics, 94 (2005) 333.

[65] S. Raynaud, E. Champion, D. Bernache-Assollant, and J. Laval, "Determination of calcium/phosphorus atomic ratio of calcium phosphate apatites using x-ray diffractometer," Journal of American Ceramic Society, 84 (2001) 359.

[66] D. Bernache-Assollanta, A. Ababoua, E. Championa, and M. Heughebaertb, "Sintering of calcium phosphate hydroxyapatite $Ca_{10}(PO_4)_6(OH)_2$ I. calcination and particle growth," Journal of European Ceramic Society, 23 (2003) 229.

[67] V. Sergey Dorozhkin, "Bioceramics of calcium orthophosphates," Biomaterials, 31 (2010) 1465.

[68] K. de Groot, editor. Bioceramics of calcium phosphate. Boca Raton, Fl: CRC Press; 1983. p.146.

[69] E. Bres and P. Hardouin, editors. Les materiaux en phosphate de calcium. Aspects fondamentaux. / calcium phosphate materials. Fundamentals. Montpellier: Sauramps Medical; (1998) p. 176.

[70] A. J. Ruys, K. A. Zeigler, O. C. Standard, A. Brandwood, B. K. Milthorpe, and C. C. Sorrel, "Hydroxyapatite sintering phenomena: densification and dehydration behaviour," in Bannister MJ, ed. Ceramics: Adding The Value, vol. 2. Proceedings of the International Ceramic Conference, Austceram 92. Melbourne: CSIRO, 1992, p. 605.

[71] A. Rus, M. Wei, C. Sorrell, M. Dickson, A. Brandwood, and B. Mitthope, "Sintering effects on the strength of hydroxyapatite," Biomaterials, 16 (1995) 409.

[72] W. L. Suchanek and M. Yoshimura, "Processing and properties of hydroxyapatite based biomaterials for use as hard tissue replacement implants," Journal of Materials Research, 13(1998) 94.

[73] L. L. Hench and E. C. Ethridge, "Biomaterials an interfacial approach," Academic Press, New York. (1982).

[74] A. Lasserre and P. K. Bajpai, "Ceramic drug-delivery devices," Critical Reviews in Therapeutic Drug Carrier Systems, 15 (1998) 1.

[75] E. A. Deutsch, K. F. Deutsch, W. P. Cacheris, W. H. Ralston, D. H. White, D. L. Nosco, R. G. Wolfangel, J. B. Wilking, L. Meeh, and S. R. Woulfe, "Treated apatite particles for x-ray diagnostic imaging," U.S. Patent No. 5,468,465 (1995).

[76] W. Huang, M. N. Rahaman, D. E. Day, and B. A. Miller, ''Strength of hollow microspheres prepared by a glass conversion process,'' Journal of Materials Science: Materials in Medicine, 20 (2009) 123.

[77] P. W. Brown and R. I. Martin, "An analysis of hydroxyapatite surface layer formation," Journal of Physical Chemistry B, 103 (1999) 1671.

[78] C. Liao, F. Lin, K. Chen, and J. Sun, "Thermal decomposition and reconstitution of hydroxyapatite in air atmosphere," Biomaterials, 20 (1999) 1807.

[79] S. J. Schneider, Jr., "Engineered Materials Handbook®: Ceramics and Glasses," ASM International (1991).

[80] X. Han and D. E. Day, "Reaction of sodium calcium borate glasses to form hydroxyapatite," Journal of Materials Science: Materials in Medicine, 18 (2007) 1837.

VITA

Gurpartap Singh Sandhu, son of Bhupinder Pal Singh Sandhu and Joginder Kaur Sandhu was born on December 7, 1985 in Karnal, India. He received his B. Tech in Mechanical Engineering from Shaheed Bhagat Singh College of Engineering and Technology, Ferozepur, Punjab, India in June 2007. Gurpartap then began pursuing his master's degree in Mechanical Engineering at Missouri University of Science and Technology, Rolla, USA under the guidance of Dr. Kimberly Henthorn, Professor of Chemical and Biological Engineering and Dr. Anthony C. Okafor, Professor of Mechanical Engineering.

During his graduate degree, Gurpartap worked as a Graduate Research Assistant with Center for Bone and Tissue Repair and Regeneration at Missouri S&T. His research was focused on synthesis and characterization of novel biodegradable microspheres for biomedical applications. Gurpartap got his Masters in Mechanical Engineering in July 2010.

Gurpartap was nominated to the engineering honor society of Tau Beta Pi in 2008. He also got certified in Lean Manufacturing Systems from Time-Wise solutions during his coursework.